



# Implicit hybridized discontinuous Galerkin methods for compressible magnetohydrodynamics



C. Ciucă<sup>a,b</sup>, P. Fernandez<sup>b,c</sup>, A. Christophe<sup>b</sup>, N.C. Nguyen<sup>b,c,\*</sup>, J. Peraire<sup>b,c</sup>

<sup>a</sup> Department of Aeronautics, Imperial College London, South Kensington Campus, London SW7 2AZ, UK

<sup>b</sup> Department of Aeronautics and Astronautics, Massachusetts Institute of Technology, 77 Massachusetts Avenue, Cambridge, MA 02139, USA

<sup>c</sup> Center for Computational Engineering, Massachusetts Institute of Technology, 77 Massachusetts Avenue, Cambridge, MA 02139, USA

## ARTICLE INFO

### Article history:

Received 11 April 2019

Received in revised form 16 September 2019

Accepted 14 October 2019

Available online 21 November 2019

### Keywords:

Finite element methods

Discontinuous Galerkin methods

Hybrid/mixed methods

Ideal and resistive magnetohydrodynamics

Divergence cleaning

Shock capturing

## ABSTRACT

We present hybridized discontinuous Galerkin (HDG) methods for ideal and resistive compressible magnetohydrodynamics (MHD). The HDG methods are fully implicit, high-order accurate and endowed with a unique feature which distinguishes themselves from other discontinuous Galerkin (DG) methods. In particular, they reduce the globally coupled unknowns to the approximate trace of the solution on element boundaries, thereby resulting in considerably smaller global degrees of freedom than other DG methods. Furthermore, we develop a shock capturing method to deal with shocks by appropriately adding artificial bulk viscosity, molecular viscosity, thermal conductivity, and electric resistivity to the physical viscosities in the MHD equations. We show the optimal convergence of the HDG methods for ideal MHD problems and validate our resistive implementation for a magnetic reconnection problem. For smooth problems, we observe that employing a generalized Lagrange multiplier (GLM) formulation can reduce the errors in the divergence of the magnetic field by two orders of magnitude. We demonstrate the robustness of our shock capturing method on a number of test cases and compare our results, both qualitatively and quantitatively, with other MHD solvers. For shock problems, we observe that an effective treatment of both the shock wave and the divergence-free constraint is crucial to ensuring numerical stability.

© 2019 Published by Elsevier Inc. This is an open access article under the CC BY-NC-ND license (<http://creativecommons.org/licenses/by-nc-nd/4.0/>).

## 1. Introduction

Discontinuous Galerkin (DG) methods [34,37,35,39,57,60] have been developed for solving MHD problems. DG methods blend desirable features of both finite volume methods and finite element methods [25], which make themselves well-suited to solving convection-dominated problems in complex geometries. In particular, DG methods deal with linear convection operators without requiring additional stabilization mechanisms, provide high-order accurate approximations, and allow for  $h/p$  refinement [26]. A common criticism of DG methods is that they have significantly more globally coupled unknowns than continuous Galerkin methods due to the duplication of degrees of freedom (DOF) on element boundaries [9], which represents a considerable disadvantage for implicit time integration. This shortcoming is addressed by hybridizable discontin-

\* Corresponding author at: Department of Aeronautics and Astronautics, Massachusetts Institute of Technology, 77 Massachusetts Avenue, Cambridge, MA 02139, USA.

E-mail addresses: [cciuca13@mit.edu](mailto:cciuca13@mit.edu) (C. Ciucă), [pablof@mit.edu](mailto:pablof@mit.edu) (P. Fernandez), [alexchri@mit.edu](mailto:alexchri@mit.edu) (A. Christophe), [cuongng@mit.edu](mailto:cuongng@mit.edu) (N.C. Nguyen), [peraire@mit.edu](mailto:peraire@mit.edu) (J. Peraire).

<https://doi.org/10.1016/j.jcpX.2019.100042>

2590-0552/© 2019 Published by Elsevier Inc. This is an open access article under the CC BY-NC-ND license (<http://creativecommons.org/licenses/by-nc-nd/4.0/>).

tinuous Galerkin (HDG) methods first in [10] for symmetric elliptic problems and later extended to other equations [46]. HDG methods inherit the desirable properties of standard DG schemes but are more efficient since the DOF on the element boundaries are uniquely defined and, as a consequence, the number of globally coupled unknowns is smaller. The embedded discontinuous Galerkin (EDG) method first proposed for elliptic problems in [24] and extended to the Navier-Stokes equations in [50,47] further reduces the number of globally coupled unknowns by making the approximate trace continuous along the element boundaries. The interior embedded discontinuous Galerkin (IEDG) method [20] employs a special approximation space for the approximate trace which is continuous for the interior faces and discontinuous for the boundary faces. This allows to eliminate DOF on the boundary faces and results in even less globally coupled DOF than EDG, but also helps improve robustness as described in [47] for the Navier-Stokes equations. The IEDG method has been successfully applied to Large-Eddy Simulations in [20,18].

Numerical simulation of compressible MHD flows with shock waves remains a challenging problem particularly for high-order discretization schemes. A number of methods rely on the non-smoothness of the numerical solution to detect shocks as well as other sharp features [31,33,51]. Among them, the sensor by Krivodonova et al. [33], devised in the context of DG methods, takes advantage of the theoretical convergence rate of DG schemes for smooth solutions in order to detect discontinuities. By construction, this sensor is limited to high-order DG methods, hyperbolic systems of conservation laws such as the Euler equations, and stabilization mechanisms that do not introduce artificial viscosity. The shock sensor by Persson et al. [51] is based on the decay rate of the coefficients of the DG polynomial approximation. Like the sensor by Krivodonova et al., it requires accuracy orders beyond about 5 to provide accurate results. Other approaches that rely on high-order derivatives of the solution include [12,11,22,28,29,41,48], but again apply only to schemes for which such derivatives can be accurately computed, such as spectral-type methods and high-order finite difference methods on structured meshes and simple geometries. Another approach is to take advantage of the strong compression that a fluid undergoes across a shock wave and use the divergence of the velocity field as a shock sensor [44,21]. PDE-based artificial viscosity approach was proposed in [3] to obtain a smooth artificial viscosity.

The MHD equations are a system of nonlinear conservation laws for the mass, momentum, energy and magnetic field together with a divergence-free constraint on the magnetic field. The exact integration of the MHD equations preserves the zero divergence of the magnetic field, if the initial condition is divergence-free. For this reason, the divergence-free condition is sometimes called an involution rather than a constraint. Unfortunately, when the MHD conservation laws are solved numerically, the divergence of the magnetic field obtained is typically not zero. It turns out that inadequate preservation of this property may lead to numerical instabilities and nonphysical features in the approximations [2,8]. Many techniques have been proposed to enforce the divergence-free condition or reduce the divergence-error in the numerical solution. They include the eight-wave methods [53], the projection method [8], the hyperbolic divergence cleaning methods [14,15], the locally divergence-free methods [36], and the constrained transport method [2,40].

In this paper, we introduce a class of hybridized discontinuous Galerkin methods for the numerical simulation of compressible magnetohydrodynamics (MHD). The HDG methods are fully implicit, high-order accurate and endowed with a unique feature which distinguishes themselves from other discontinuous Galerkin (DG) methods. In particular, they reduce the globally coupled unknowns to the approximate trace of the solution on element boundaries, thereby resulting in considerably smaller global degrees of freedom than other DG methods. Typically, other DG methods [37,35,39,57,60] for MHD use explicit time integration and have timestep size limited by the CFL condition. HDG methods use implicit time integration and thus can take much larger timestep size at the expense of solving nonlinear systems of equations. Hence, HDG methods are well-suited to viscous MHD as well as problems that require small elements to adequately resolve physics. Although HDG methods have been used to solve incompressible MHD [34], they are not yet applied to compressible viscous MHD. Furthermore, we develop a shock capturing method to deal with shocks, contact discontinuities, and other unresolved features (such as strong current sheets, shear layers and thermal gradients). Our shock capturing method is an extension of the previous work [44,21] and based on the addition of physics-based artificial bulk viscosity, molecular viscosity, thermal conductivity, and electric resistivity to the MHD equations. We validate the HDG methods on a number of smooth problems and demonstrate the robustness of our shock capturing method on a number of test cases and compare our results, both qualitatively and quantitatively, with other MHD solvers. For shock problems, we show that enforcing the divergence to be small using a Lagrange multiplier becomes an essential step in ensuring numerical stability.

The paper is organized as follows. In Section 2, we introduce partial differential equations governing magnetohydrodynamics. Next, we describe hybridized DG methods in Section 3 and shock capturing in Section 4. In Section 5, we apply these methods to a variety of MHD problems and discuss the results. In Section 6, we end the paper with a summary of the results and concluding remarks on future work.

## 2. Magnetohydrodynamics

### 2.1. Formulation

The set of partial differential equations governing MHD describe the dynamic effects of magnetic fields in electrically conducting fluids [16]. Here, we will consider compressible MHD [7] and assume that the plasma is collisionless and that an extended equation of state for an ideal gas holds. In addition, we will neglect relativistic effects. For simplicity of illustration, we set the permeability to unity. Hence, the equations of interest can be written in the following non-dimensional form:

$$\frac{\partial \mathbf{U}}{\partial t} + \nabla \cdot \mathbf{F}(\mathbf{U}) - \nabla \cdot \mathbf{G}(\mathbf{U}, \nabla \mathbf{U}) = \mathbf{S}(\mathbf{U}, \nabla \mathbf{U}) \quad (1)$$

where  $\mathbf{U} := (\rho, \rho \mathbf{u}, E, \mathbf{B})^\top$  is the vector of conserved dimensionless variables and  $\rho$  is the density,  $E$  the total specific energy,  $\mathbf{u} = (u_x, u_y, u_z)^\top$  is the fluid velocity and  $\mathbf{B} = (B_x, B_y, B_z)^\top$ , the magnetic induction. The non-linear inviscid flux is given by:

$$\mathbf{F}(\mathbf{U}) = \begin{bmatrix} \rho \mathbf{u} \\ \rho \mathbf{u} \otimes \mathbf{u} + (p + \frac{1}{2} |\mathbf{B}|^2) \mathbb{I} - \mathbf{B} \otimes \mathbf{B} \\ (E + p + \frac{1}{2} |\mathbf{B}|^2) \mathbf{u} - \mathbf{B} (\mathbf{u} \cdot \mathbf{B}) \\ \mathbf{u} \otimes \mathbf{B} - \mathbf{B} \otimes \mathbf{u} \end{bmatrix} \quad (2)$$

where the hydrodynamic pressure  $p$  is obtained from the equation of state for an ideal gas:

$$p = (\gamma - 1) \left( E - \frac{1}{2} \rho |\mathbf{u}|^2 - \frac{1}{2} |\mathbf{B}|^2 \right). \quad (3)$$

The viscous, resistive flux vector can be expressed as [13]:

$$\mathbf{G}(\mathbf{U}, \nabla \mathbf{U}) = \begin{bmatrix} 0 \\ \frac{1}{S_v} \boldsymbol{\tau} \\ \frac{1}{S_v} \boldsymbol{\tau} \cdot \mathbf{u} + \frac{\gamma}{\gamma-1} \frac{1}{Pr S_v} \nabla T - \frac{1}{S_r} ((\nabla \times \mathbf{B}) \times \mathbf{B}) \\ \frac{1}{S_r} ((\nabla \mathbf{B})^\top - \nabla \mathbf{B}) \end{bmatrix} \quad (4)$$

where  $\boldsymbol{\tau} = (\nabla \mathbf{u})^\top + \nabla \mathbf{u} + \left( \frac{\beta}{\mu} - \frac{2}{3} \right) (\nabla \cdot \mathbf{u}) \mathbb{I}$  is the viscous stress tensor,  $S_v$  is the viscous Lundquist number,  $Pr$  the Prandtl number,  $\gamma$  the adiabatic exponent and  $S_r$  the resistive Lundquist number. We also note that  $\beta$  is the bulk viscosity and  $\mu$  the dynamic viscosity. The dimensionless temperature becomes  $T = p/\rho$ . The exact solution of the MHD system (1) satisfies the solenoidal condition

$$\nabla \cdot \mathbf{B} = 0 \quad (5)$$

which expresses the lack of experimentally observed magnetic monopoles [4]. Finally, the source term is

$$\mathbf{S}(\mathbf{U}, \nabla \mathbf{U}) = - \begin{bmatrix} 0 \\ (\nabla \cdot \mathbf{B}) \mathbf{B} \\ (\nabla \cdot \mathbf{B}) \mathbf{u} \cdot \mathbf{B} \\ (\nabla \cdot \mathbf{B}) \mathbf{u} \end{bmatrix}, \quad (6)$$

which can be considered zero because of the solenoidal condition (5). The derivation of the conservative form (1) can be found in [15].

Godunov [23] first noticed that the MHD system is not symmetrizable. This means that a pair of entropy variables and entropy fluxes cannot be found for the ideal and resistive MHD systems [4]. The symmetric form of the ideal MHD equations, as proposed initially by Godunov [23], relies on adding the source term:  $\mathbf{S} = -\nabla \cdot \mathbf{B} (0, \mathbf{B}, \mathbf{u} \cdot \mathbf{B}, \mathbf{u})^\top$ , which is zero for the exact solution. However, we note that the added source terms are non-conservative, and this may potentially lead to numerical difficulties in the presence of discontinuities [58]. It is important to point out that we do not encounter numerical difficulties even in the presence of shocks when the non-conservative source terms are added. This demonstrates the robustness of our shock capturing method.

## 2.2. The solenoidal involution

We note that the last equation in (1) is derived from the generalized Ohm's law  $\mathbf{E} + \mathbf{u} \times \mathbf{B} = \eta \mathbf{J}$ , the Maxwell–Ampère equation  $\nabla \times \mathbf{B} = \mu_0 \mathbf{J}$ , and the Maxwell–Faraday equation:

$$\frac{\partial \mathbf{B}}{\partial t} + \nabla \times \mathbf{E} = 0. \quad (7)$$

Taking the divergence of equation (7) and noting that the divergence of the curl of a vector field is zero, we see that if the initial condition for the magnetic field satisfies (5), then the solution will remain divergence-free for all times. However, because the numerical discretization of the equation (7) is not exact [14], equation (5) will not be satisfied exactly by a numerical scheme. The implications are the following [2,8]: the divergence-free errors tend to increase with time and may lead to simulation breakdown. They may result in non-physical solution in which magnetic field lines may have wrong topologies, leading to plasma transport orthogonal to the magnetic field lines [32]. In our experience, these errors become a more serious issue for non-smooth problems which exhibit shocks and contact discontinuities.

Many techniques have been proposed to enforce the divergence-free condition or reduce the divergence error in numerical simulations. Constrained transport methods [2,40] modifies the discretization of the magnetic induction equation to satisfy exactly  $\nabla \cdot \mathbf{B} = 0$ . However, these changes might negatively affect other desirable properties of the underlying scheme, also requiring structured grids and large stencils [58]. Another method [8], relies on projecting the magnetic field in the space of zero divergence vectors, which requires the solution of a Poisson equation to correct the magnetic field. The method developed by Powell [53] is based on the symmetric form of the MHD equations and employs the stabilizing source terms as well as using a Roe-type solver admitting normal jumps in the magnetic field at the element interfaces. Another possibility in the context of DG methods is to construct locally divergence free approximations for the magnetic field [36], which seems to perform well for smooth problems. An imposition of the divergence-free constraint presented in [30] employs a preprocessing step for the local error, and Dedner's generalized Lagrange multiplier formulation [14] for both the global and the local errors.

The method used in this paper follows the GLM approach introduced in [14]. In particular, we consider the GLM-MHD formulation recently proposed by Derigs' et al. [15]:

$$\frac{\partial}{\partial t} \begin{bmatrix} \rho \\ \rho \mathbf{u} \\ E \\ \mathbf{B} \\ \psi \end{bmatrix} + \nabla \cdot \begin{bmatrix} \rho \mathbf{u} \\ \rho (\mathbf{u} \otimes \mathbf{u}) + (p + \frac{1}{2} |\mathbf{B}|^2) \mathbb{I} - \mathbf{B} \otimes \mathbf{B} \\ \mathbf{u} \left( \frac{1}{2} \rho |\mathbf{u}|^2 + \frac{\gamma p}{\gamma - 1} + |\mathbf{B}|^2 \right) - \mathbf{B} (\mathbf{u} \cdot \mathbf{B}) + c_h \psi \\ \mathbf{u} \otimes \mathbf{B} - \mathbf{B} \otimes \mathbf{u} + c_h \psi \mathbb{I} \\ c_h \mathbf{B} \end{bmatrix} = - \begin{bmatrix} 0 \\ (\nabla \cdot \mathbf{B}) \mathbf{B} \\ (\nabla \cdot \mathbf{B}) \mathbf{u} \cdot \mathbf{B} \\ (\nabla \cdot \mathbf{B}) \mathbf{u} \\ \alpha \psi \end{bmatrix} \quad (8)$$

together with

$$p = (\gamma - 1) \left( E - \frac{1}{2} \rho |\mathbf{u}|^2 - \frac{1}{2} |\mathbf{B}|^2 - \frac{1}{2} \psi^2 \right). \quad (9)$$

The unknown scalar  $\psi$  has been introduced to couple equation (5) to the system (1). Furthermore, we consider the following formula for the *hyperbolic divergence cleaning speed*  $c_h$ :

$$c_h = \sqrt{\lambda_{\max} (\lambda_{\max} - u_{\max, \Omega})}, \quad (10)$$

where  $\lambda_{\max}$  denotes the largest eigenvalue of the Jacobian  $\mathbb{A} = (\partial \mathbf{F} / \partial \mathbf{U}) \cdot \mathbf{n}$  and  $u_{\max, \Omega} = \max_{\Omega} (|u_x|, |u_y|, |u_z|)$  is the largest speed in the entire physical domain. Numerical experiments in [15] suggest that the best choice of  $\alpha$  depends on the boundary conditions. A choice of  $\alpha = 2$  works well for periodic boundary conditions.

### 2.3. Hyperbolicity

The system of partial differential equations that describes ideal magnetohydrodynamics is hyperbolic, whereas the system that describes resistive MHD is of mixed parabolic-hyperbolic type. The one dimensional ideal MHD system admits 7 distinct wave systems whose speeds are [54]:

$$\lambda_{\pm f}^x = u_x \pm c_f, \quad \lambda_{\pm s}^x = u_x \pm c_s, \quad \lambda_{\pm a}^x = u_x \pm c_A, \quad \lambda_E^x = u_x \quad (11)$$

with

$$c_A^2 = b_x^2, \quad c_{f,s}^2 = \frac{1}{2} \left( a^2 + |\mathbf{b}|^2 \pm \sqrt{(a^2 + |\mathbf{b}|^2)^2 - 4a^2 b_x^2} \right), \quad \mathbf{b} = \frac{\mathbf{B}}{\sqrt{\rho}}, \quad a^2 = \gamma \frac{p}{\rho} \quad (12)$$

where  $a$  is the speed of sound of an ideal gas,  $c_A$  is the Alfvén wave speed, and  $c_f$  and  $c_s$  are the fast and slow magnetoacoustic wave speeds. Besides the fast, slow and Alfvén waves, the last eigenvalue corresponds to the speed of the entropy wave. If we add the non-conservative source terms we obtain Powell's eight-wave formulation [53]. If we add  $\psi$  as in equation (8), the eighth and ninth wave speed take the form:

$$\lambda_{\pm \psi}^x = \frac{1}{2} u_x \pm \frac{1}{2} \sqrt{u_x^2 + 4c_h^2}. \quad (13)$$

The extension to higher dimensions is straightforward if we consider the Riemann problem at each shared element interface, and the  $x$  direction is replaced by the direction normal to the element interface.

## 3. Hybridized DG methods

### 3.1. Approximation spaces

The hybridized DG framework is based on the previous work [20] for the Euler and Navier-Stokes equations. Let  $m$  denote the number of conserved variables and  $d$  the number of spatial dimensions of the problem. Let  $\mathcal{T}_h$  be the discretization of

the domain  $\Omega$  into disjoint elements  $K$ , and  $\partial\mathcal{T}_h := \{\partial K : K \in \mathcal{T}_h\}$  the set of element boundaries. Let  $\mathcal{E}_h^0$  and  $\mathcal{E}_h^\partial$  be the set of interior faces and boundary faces, respectively, with  $\mathcal{E}_h$  their union. Furthermore, let  $\mathcal{P}_k(D)$  be the space of polynomials of degree at most  $k$  on domain  $D \subset \mathbb{R}^n$ , and let  $L^2(D)$  be the space of square integrable functions on  $D$ , and  $C^0(D)$  the space of continuous functions on  $D$ . Also, let  $\boldsymbol{\psi}_K^p$  denote the  $p$ -th degree parametric mapping from the reference element  $K_{ref}$  to an element  $K \in \mathcal{T}_h$ , and let  $\boldsymbol{\phi}_F^p$  denote the  $p$ -th degree parametric mapping from the reference face  $F_{ref}$  to a face  $F \in \mathcal{E}_h$ . Isoparametric mapping  $p = k$  is used throughout this paper. We introduce the following finite element discontinuous spaces: the space of approximate solutions

$$\mathbf{W}_h^k = \left\{ \mathbf{w} \in \left( L^2(\mathcal{T}_h) \right)^m : (\mathbf{w} \circ \boldsymbol{\psi}_K^p)|_K \in (\mathcal{P}_k(K_{ref}))^m, \quad \forall K \in \mathcal{T}_h \right\}, \quad (14)$$

the space of the approximate solution gradients

$$\mathbf{V}_h^k = \left\{ \mathbf{v} \in \left( L^2(\mathcal{T}_h) \right)^{m \times d} : (\mathbf{v} \circ \boldsymbol{\psi}_K^p)|_K \in (\mathcal{P}_k(K_{ref}))^{m \times d}, \quad \forall K \in \mathcal{T}_h \right\} \quad (15)$$

and the space of the approximate trace of the solution

$$\mathbf{M}_h^k = \left\{ \boldsymbol{\mu} \in \left( L^2(\mathcal{E}_h) \right)^m : (\boldsymbol{\mu} \circ \boldsymbol{\phi}_F^p)|_F \in (\mathcal{P}_k(F_{ref}))^m, \quad \forall F \in \mathcal{E}_h, \text{ and } \boldsymbol{\mu}|_{\mathcal{E}_h^E} \in \left( C^0(\mathcal{E}_h^E) \right)^m \right\}. \quad (16)$$

The choice of  $\mathcal{E}_h^E$  dictates the hybridized method: choosing  $\mathcal{E}_h^E = \emptyset$  results in the HDG method, choosing  $\mathcal{E}_h^E = \mathcal{E}_h$  results in the EDG method, while  $\mathcal{E}_h^E = \mathcal{E}_h^0$  leads to the IEDG method.

Finally, we define the following inner products: for  $\mathbf{a}, \mathbf{b} \in (L^2(D))^m$  we have  $(\mathbf{a}, \mathbf{b})_D = \int_D \mathbf{a} \cdot \mathbf{b}$  if  $D \subset \mathbb{R}^d$  and  $(\mathbf{a}, \mathbf{b}) = \int_D \mathbf{a} \cdot \mathbf{b}$  if  $D \subset \mathbb{R}^{d-1}$ . For  $\mathbf{A}, \mathbf{B} \in (L^2(D))^{m \times d}$  we have  $(\mathbf{A}, \mathbf{B})_D = \int_D \text{tr}(\mathbf{A}^T \mathbf{B})$  if  $D \subset \mathbb{R}^d$  and  $(\mathbf{A}, \mathbf{B}) = \int_D \text{tr}(\mathbf{A}^T \mathbf{B})$  if  $D \subset \mathbb{R}^{d-1}$ , where  $\text{tr}(\cdot)$  denotes the trace operator.

### 3.2. First-order MHD systems

We describe the backward Euler scheme for temporal discretization. The generalization to backward difference formulae and diagonally implicit Runge-Kutta schemes is straightforward. For a first-order MHD system such as the GLM-MHD formulation (8) augmented with proper initial and boundary conditions, we discretize the time derivative with the backward Euler scheme to find the approximation  $(\mathbf{U}_h^n, \widehat{\mathbf{U}}_h^n) \in \mathbf{W}_h^k \times \mathbf{M}_h^k$  such that

$$\begin{aligned} \left( \frac{\mathbf{U}_h^n}{\Delta t}, \mathbf{w} \right)_{\mathcal{T}_h} - (\mathbf{F}(\mathbf{U}_h^n), \nabla \mathbf{w})_{\mathcal{T}_h} + (\widehat{\mathbf{F}}_h^n, \mathbf{w})_{\partial\mathcal{T}_h} &= \left( \frac{\mathbf{U}_h^{n-1}}{\Delta t}, \mathbf{w} \right)_{\mathcal{T}_h} + (\mathbf{S}, \mathbf{w})_{\mathcal{T}_h}, \quad \forall \mathbf{w} \in \mathbf{W}_h^k \\ (\widehat{\mathbf{F}}_h^n, \boldsymbol{\mu})_{\partial\mathcal{T}_h \setminus \partial\Omega} + (\widehat{\mathbf{B}}_h^n, \boldsymbol{\mu})_{\partial\Omega} &= 0, \quad \forall \boldsymbol{\mu} \in \mathbf{M}_h^k \end{aligned} \quad (17)$$

where

$$\widehat{\mathbf{F}}_h^n(\mathbf{U}_h^n, \widehat{\mathbf{U}}_h^n) = \mathbf{F}(\widehat{\mathbf{U}}_h^n) \cdot \mathbf{n} + \mathbb{S}(\mathbf{U}_h^n, \widehat{\mathbf{U}}_h^n)(\mathbf{U}_h^n - \widehat{\mathbf{U}}_h^n) \quad (18)$$

and  $\widehat{\mathbf{B}}_h$  is the boundary flux for enforcing the boundary conditions and  $\mathbf{S}(\mathbf{U}_h^n)$  is the source term. The stabilization matrix  $\mathbb{S}$  is chosen either according to the Lax-Friedrich (LF) method

$$\mathbb{S} = \lambda_{\max} \mathbb{I}. \quad (19)$$

In the current work, we use a global Lax-Friedrich method

$$\lambda_{\max}(\Omega) = \sup_{\mathbf{x} \in \Omega} \lambda_{\max}(\mathbf{x}) \quad (20)$$

We consider two options: computing  $\lambda_{\max}$  based on the initial conditions and keeping it constant throughout the simulation or recomputing  $\lambda_{\max}$  at the beginning of each time step. For the test cases presented here, we observe no added benefit in terms of accuracy or stability with the second option.

The system of equations (17) is linearized by using Newton's method to yield the following linear system:

$$\begin{bmatrix} A & B \\ C & D \end{bmatrix} \begin{pmatrix} U \\ \Lambda \end{pmatrix} = \begin{pmatrix} F \\ G \end{pmatrix} \quad (21)$$

where  $U$  and  $\Lambda$  are the DOFs associated with  $\mathbf{U}_h$  and  $\widehat{\mathbf{U}}_h$  respectively. Due to the discontinuous finite element spaces, the matrix  $A$  has a block diagonal structure, and hence can be easily inverted, leaving us to solve the global system

$$\mathbb{K} \Lambda = \mathbb{R} \quad (22)$$

where the stiffness matrix  $\mathbb{K}$  and the residual  $\mathbb{R}$  can be easily obtained from (21) by inverting  $A$  and eliminating  $U$ . The linear system (22) is solved by using the GMRES method and block-ILU additive Schwarz preconditioner [20].

### 3.3. Second-order MHD systems

To solve second-order MHD systems, such as the ideal GLM-MHD system with non-conservative source terms (8) or the resistive MHD equations (1), we introduce the additional variable  $\mathbf{Q}$  and the additional equation:

$$\mathbf{Q} - \nabla \mathbf{U} = 0, \quad \text{in } \Omega \quad (23)$$

At every timestep  $n$ , we find an approximation  $(\mathbf{Q}_h^n, \mathbf{U}_h^n, \widehat{\mathbf{U}}_h^n) \in \mathbf{V}_h^k \times \mathbf{W}_h^k \times \mathbf{M}_h^k$  such that

$$\begin{aligned} (\mathbf{Q}_h^n, \mathbf{v})_{\mathcal{T}_h} + (\mathbf{U}_h^n, \nabla \cdot \mathbf{v})_{\mathcal{T}_h} - \langle \widehat{\mathbf{U}}_h^n, \mathbf{v} \cdot \mathbf{n} \rangle_{\partial \mathcal{T}_h} &= 0, & \forall \mathbf{v} \in \mathbf{V}_h^k \\ \left( \frac{\mathbf{U}_h^n}{\Delta t}, \mathbf{w} \right)_{\mathcal{T}_h} - (\mathbf{F} + \mathbf{G}, \nabla \mathbf{w})_{\mathcal{T}_h} + \langle \widehat{\mathbf{F}}_h^n + \widehat{\mathbf{G}}_h^n, \mathbf{w} \rangle_{\partial \mathcal{T}_h} &= \left( \frac{\mathbf{U}_h^{n-1}}{\Delta t}, \mathbf{w} \right)_{\mathcal{T}_h} + (\mathbf{S}, \mathbf{w})_{\mathcal{T}_h}, & \forall \mathbf{w} \in \mathbf{W}_h^k \\ \langle \widehat{\mathbf{F}}_h^n + \widehat{\mathbf{G}}_h^n, \boldsymbol{\mu} \rangle_{\partial \mathcal{T}_h \setminus \partial \Omega} + \langle \widehat{\mathbf{B}}_h^n, \boldsymbol{\mu} \rangle_{\partial \Omega} &= 0, & \forall \boldsymbol{\mu} \in \mathbf{M}_h^k \end{aligned} \quad (24)$$

where

$$\widehat{\mathbf{F}}_h^n(\mathbf{U}_h^n, \widehat{\mathbf{U}}_h^n) = \mathbf{F}(\widehat{\mathbf{U}}_h^n) \cdot \mathbf{n} + \mathbb{S}(\mathbf{U}_h^n, \widehat{\mathbf{U}}_h^n)(\mathbf{U}_h^n - \widehat{\mathbf{U}}_h^n) \quad (25)$$

and

$$\widehat{\mathbf{G}}_h^n(\widehat{\mathbf{U}}_h^n, \mathbf{Q}_h^n) = \mathbf{G}(\widehat{\mathbf{U}}_h^n, \mathbf{Q}_h^n) \cdot \mathbf{n}. \quad (26)$$

In (24),  $\mathbf{F}$ ,  $\mathbf{G}$ ,  $\mathbf{S}$  stand for  $\mathbf{F}(\mathbf{U}_h^n)$ ,  $\mathbf{G}(\mathbf{U}_h^n, \mathbf{Q}_h^n)$ ,  $\mathbf{S}(\mathbf{U}_h^n, \mathbf{Q}_h^n)$ . We note that  $\mathbb{S}$ , while based on the inviscid flux, is used to stabilize both  $\mathbf{F}$  and  $\mathbf{G}$  (given the linear addition) and this was found to work well for the cases presented here. For other cases, a viscous  $\mathbb{S}$  might be required. The nonlinear system (24) is solved using the same solution procedure described in the previous section.

## 4. Shock capturing

### 4.1. Hydrodynamics

To deal with shocks and other types of discontinuity, we extend the physics-based approach introduced by Fernandez et al. [21,19] for the hydrodynamics. This approach relies on shock, thermal gradient and shear sensors. The *shock sensor* is constructed such that

$$s_\beta(\mathbf{x}) = s_\theta \cdot s_\omega, \quad s_\theta = -\frac{h_\beta}{k} \frac{\nabla \cdot \mathbf{u}}{a^*}, \quad s_\omega = \frac{(\nabla \cdot \mathbf{u})^2}{(\nabla \cdot \mathbf{u})^2 + |\nabla \times \mathbf{u}|^2 + \varepsilon}, \quad (27)$$

where  $\varepsilon$  is a constant of the order of the machine precision,  $k$  is the polynomial degree and  $a^*$  is the critical speed of sound. The element size is taken along the direction of the density gradient

$$h_\beta(\mathbf{x}) = h_{\text{ref}} \frac{|\nabla \rho|}{\sqrt{\nabla \rho^T \cdot \mathbf{M}_h^{-1} \nabla \rho} + \varepsilon} \quad (28)$$

where  $\mathbf{M}_h$  is the metric tensor of the mesh (see [38,61] for details), and  $h_{\text{ref}}$  is the size of the reference element used in the construction of  $\mathbf{M}_h$ . A smooth min-max function is used to bound the sensor between 0 and  $2/\sqrt{\gamma^2 - 1}$ . The upper bound comes from analysis for stationary 1D shocks [19].

The *thermal sensor* is designed to detect under-resolved thermal gradient and is constructed from

$$s_\kappa(\mathbf{x}) = \frac{h_{\text{ref}} |\nabla_\xi T|}{k T_0} \quad (29)$$

where  $T_0$  is the stagnation temperature and  $\nabla_\xi T$  is the temperature gradient in the reference element coordinates  $\xi$ ,

$$\nabla_\xi T = \frac{\partial T}{\partial \xi_i} = \sum_{j \leq d} \frac{\partial T}{\partial \mathbf{x}_j} \frac{\partial \mathbf{x}_j}{\partial \xi_i}, \quad i = 1, \dots, d. \quad (30)$$

The *shear sensor* is designed to detect under-resolved velocity gradient and is constructed from

$$s_\mu(\mathbf{x}) = \frac{h_{\text{ref}} \|\mathcal{L}(\mathbf{u}) \cdot \mathbf{x}_\xi^T\|_2}{k u_{\text{max}}} \quad (31)$$

where  $\|\cdot\|_2$  denotes the Euclidean norm,  $u_{\text{max}}$  is the maximum isentropic velocity

$$u_{\max} = \sqrt{|\mathbf{u}|^2 + \frac{2}{\gamma - 1} a^2}, \quad \mathcal{L}(\mathbf{u}) = \frac{\partial \mathbf{u}_i}{\partial \mathbf{x}_j} (1 - \delta_{ij}). \quad (32)$$

Both the thermal sensor and the shear sensor are smoothly bounded between 0 and 2.

Inspired by previous work [1,12,11,22,28,29,41,48], Fernandez et al. [21,19] add artificial bulk viscosity, thermal conductivity and molecular viscosity ( $\beta^*$ ,  $\kappa^*$ ,  $\mu^*$ ) to the physical values such that:

$$\beta = \beta_f + \beta^*, \quad \kappa = \kappa_f + \kappa^* = \kappa_f + \kappa_1^* + \kappa_2^*, \quad \mu = \mu_f + \mu^*,$$

where the artificial viscosities are determined to ensure a cell Péclet number of  $\mathcal{O}(1)$  as follows

$$\beta^*(\mathbf{x}) = \hat{s}_\beta \rho \frac{k_\beta h_\beta}{k} \sqrt{|\mathbf{u}|^2 + a^{*2}} \quad (33a)$$

$$\kappa^*(\mathbf{x}) = \hat{s}_\beta \rho \frac{c_p}{Pr_\beta^*} \frac{k_\beta h_\beta}{k} \sqrt{|\mathbf{u}|^2 + a^{*2}} + \hat{s}_\kappa \rho c_p \frac{k_\kappa h_\kappa}{k} \sqrt{|\mathbf{u}|^2 + a^{*2}} \quad (33b)$$

$$\mu^*(\mathbf{x}) = \hat{s}_\mu \rho \frac{k_\mu h_\mu}{k} \sqrt{|\mathbf{u}|^2 + a^{*2}}. \quad (33c)$$

Here  $k_{\mu,\kappa} = 1$ ,  $k_\beta = 1.5$ , and  $Pr_\beta^*$  is an artificial Prandtl number relating  $\beta^*$  to  $\kappa_1^*$  (in the current work  $Pr_\beta^* = 0.9$ ). Note that  $(\hat{s}_\beta, \hat{s}_\kappa, \hat{s}_\mu)$  denote the smoothly bounded values of the sensors in equations (27), (29) and (31) (see [19] for details). We also note that

$$h_\kappa(\mathbf{x}) = h_{\text{ref}} \frac{|\nabla T|}{\sqrt{\nabla T^T \cdot \mathbf{M}_h^{-1} \nabla T + \varepsilon}}, \quad h_\mu(\mathbf{x}) = h_{\text{ref}} \inf_{|\mathbf{a}|=1} \left\{ \mathbf{a}^T \cdot \mathbf{M}_h \mathbf{a} \right\}. \quad (34)$$

Finally, a smoothing operator is applied to  $(\beta^*, \kappa^*, \mu^*)$  to make all 3 fields  $\mathcal{C}^0$  continuous [19]. Since moderate orders are used for the numerical examples in this paper, we employ an element-wise linear reconstruction procedure introduced in [45] for the element size.

#### 4.2. Extension to MHD problems

To extend the above approach to MHD, we use  $\beta^*$ ,  $\kappa^*$ ,  $\mu^*$  as introduced in equation (33) with the following modifications. First, instead of the critical sound speed  $a^*$  we use  $c_f^*$ , where the critical fast wave speed  $c_f^*$  is computed based on equation (11) by replacing  $a$  with  $a^*$ . Note that in the case of zero magnetic induction, the fast wave speed reduces to the speed of sound. Second, wherever pressure comes into the computations (such as when computing  $a$ ) we have used the GLM-MHD pressure, given by equation (9). And third, we further introduce an artificial resistivity, such that  $\eta = \eta_f + \eta^*$ . This new artificial dissipation mechanism is necessary to stabilize both shocks and under-resolved features for MHD problems.

To construct  $\eta^*$ , we introduce the resistivity sensor as follows

$$s_\eta = \frac{h_\eta}{k} \frac{|\mathbf{J}|}{2\sqrt{\pi}|\mathbf{B}|} \quad (35)$$

where the element size is taken in the direction of the gradient of the magnetic pressure ( $p_m = \frac{|\mathbf{B}|^2}{2}$ ), as suggested by Kawai [27]:

$$h_\eta(\mathbf{x}) = h_{\text{ref}} \frac{|\nabla p_m|}{\sqrt{\nabla p_m^T \cdot \mathbf{M}_h^{-1} \nabla p_m + \varepsilon}}. \quad (36)$$

Our use of the euclidean norm of the current density  $\mathbf{J} = \nabla \times \mathbf{B}$  as a shock indicator is, again, inspired by Kawai's choice of indicator  $|\mathbf{J}|^2$  [27]. Division by  $2\sqrt{\pi}|\mathbf{B}|$  in equation (35) is done to ensure both thermodynamic consistency, where the choice of non-dimensionalisation relies on [13]:

$$E_0 = p_0 = \frac{B_0^2}{8\pi} = \frac{\rho_0 c_A^2}{2} \quad (37)$$

and dimensional consistency ( $s_\eta$  is dimensionless and of  $\mathcal{O}(1)$ ). Finally, the artificial resistivity is given by

$$\eta^*(\mathbf{x}) = \hat{s}_\eta \frac{k_\eta h_\eta}{k} \sqrt{|\mathbf{u}|^2 + c_f^{*2}} \quad (38)$$

where  $k_\eta = 1.8$  (empirically chosen) and  $\hat{s}_\eta$  represents the smoothly bounded value of  $s_\eta$  between 0 and 2. Note that the same linear reconstruction [45] is used to make  $\eta^*$  continuous across elements.

## 5. Results

In this section we present several examples to verify the optimal convergence of our hybridized DG schemes and demonstrate the robustness of the proposed shock capturing method on MHD problems with shock waves. In order to assess the magnitude of the divergence errors, we use the following measure: the  $L^2$  norm  $\|\nabla \cdot \mathbf{B}_h\|_{L^2(\mathcal{T}_h)}$ , and the sum of the absolute value of the normal jumps of the magnetic field vector across element interfaces  $\sum_{F \in \mathcal{E}_h} \int_F |[\![\mathbf{B}_h]\!]| ds$ .

### 5.1. Smooth Alfvén waves

We use this first test case to show the optimal convergence of our HDG scheme on triangular elements for polynomial degrees  $k = 1, 2, 3$ , and to compare Dedner's [14] and Derigs' [15] GLM formulations. We also use this smooth problem to investigate the errors in the divergence of the magnetic field, and the effectiveness of the Lagrange multiplier approach for divergence cleaning.

The circularly polarized Alfvén waves are analytic solutions to the nonlinear ideal MHD equations. The test case we use is the same as the one used by Toth [58]. We consider a wave travelling at an incidence  $\alpha = 30^\circ$  over the rectangular domain defined by  $\Omega = [0, 1/\cos\alpha] \times [0, 1/\sin\alpha]$  with periodic boundary conditions. The wave period is  $T = 1$  and the initial conditions are defined as:  $\rho = 1$ ,  $v_{\parallel} = 0$ ,  $p = 0.1$ ,  $B_{\parallel} = 1$ ,  $v_{\perp} = 0.1 \sin[2\pi(x \cos\alpha + y \sin\alpha)] = B_{\perp}$  and  $v_z = 0.1 \cos[2\pi(x \cos\alpha + y \sin\alpha)] = B_z$ . We note that the subscripts  $\parallel$  and  $\perp$  denote the directions parallel and perpendicular to the wave travelling direction, respectively.

We first discretize the rectangular domain into  $N \times N$  rectangles, which are then each split into 2 triangular elements. We use the notation  $h = 1/N$  and show optimal convergence (order  $k + 1$ ) for all conserved variables in Table 1, for Dedner's formulation. Table 2 compares Dedner's ideal GLM-MHD [14] to Derigs' ideal GLM-MHD [15]. While the differences are small, Derigs' version seems to consistently produce smaller errors. We recover the same optimal convergence order in Derig's formulation irrespective of whether we include the Godunov source terms or not, with very similar errors. In Table 3 we show the errors in the divergence of the magnetic field with and without divergence cleaning. We note that using Derigs' GLM method reduces the divergence error by one order of magnitude. As expected, for all formulations the divergence errors decrease with increasing polynomial order. Also, we observe that varying  $\alpha$  adds no advantage, while increasing  $c_h$  can result in further reducing by another order of magnitude the divergence error. While for explicit schemes the CFL condition prevents  $c_h$  from being increased to the values shown in Table 3 [14], for our method this is not a problem. We note however, that increasing  $c_h$  means that we have to increase  $\lambda_{\max}$  to stabilize our scheme, via equation (13) and this has a negative effect on the conditioning property of the system: for example, increasing  $c_h$  by a factor of 100 means 9 times more GMRES iterations to converge to the same residual value. Hence, we conclude that divergence cleaning is warranted even for smooth problems and  $c_h$  should be chosen appropriately.

### 5.2. Smooth magnetic vortex

In this example, we show the optimal convergence of all three of our schemes (HDG, EDG and IEDG) for quadrilateral elements. We compare the errors between the three formulations and remark on their robustness for both quadrilateral and triangular elements. Note that from this problem onwards we will use Derigs' GLM formulation for controlling the divergence error since we observe no significant difference between Derigs' GLM formulation and Dedner's formulation [14] for non-smooth problems, while the former yields consistently slightly smaller errors than the latter for smooth problems.

The iso-density MHD vortex [42,17] computational domain is defined in the domain  $\Omega = [-5, 5]^2$  with periodic boundary conditions. The initial conditions are given as  $\rho = 1$ ,  $\mathbf{u} = \mathbf{1} + (-y, x, 0) \mu e^{q(1-r^2)}$ , while  $\mathbf{B} = (-y, x, 0) \mu e^{q(1-r^2)}$  and  $p = 1 + 1/(4q) \left[ \mu^2 (1 - 2qr^2) \kappa e^{q(1-r^2)} \right]$ . The constants  $\kappa$  and  $\mu$  are set to  $1/(2\pi)$ ,  $r = \sqrt{x^2 + y^2}$  and  $q = 0.5$  for  $k = 1$  and  $q = 1$  for  $k \geq 2$  [42]. The analytic solution consists of the simple diagonal advection of the vortex with period  $T = 10$ .

We discretize the domain into  $N \times N$  quadrilateral elements. We show optimal convergence for the magnetic induction for all three schemes and  $k = 1, 2, 3$  in Table 4. We can notice that for  $k \geq 2$  we achieve optimal convergence and for  $k = 1$  we achieve super-convergence (order  $k + 2$ ). This super-convergence for this problem for  $k = 1$  has also been observed by other authors [60]. For  $k = 1$ , both HDG and IEDG are more accurate than EDG. For  $k \geq 2$ , the differences among HDG, EDG, and IEDG are very small. We conclude that IEDG is the most efficient method because it has similar accuracy as HDG and similar DOF as EDG.

### 5.3. GEM reconnection challenge

The GEM (Geospace Environmental Modelling) Reconnection challenge was first proposed in [5] as a means to test the ability of numerical codes to capture the phenomenon of magnetic reconnection, as well as a means of comparison between codes implementing different models (e.g. resistive MHD, Hall MHD). Magnetic reconnection represents the breaking of the frozen-in condition due to resistive effects, where field lines break and reconnect, altering the topology of the magnetic field. This is a common MHD phenomenon and occurs in solar flares, the Earth's magnetosphere and tokamaks, starting

**Table 1**

History of numerical errors and convergence orders for the HDG-GLM-MHD formulation for the polarized Alfvén wave problem at  $T = 1$ . Time integration is carried out using a DIRK(3,3) scheme for  $k = 1, 2$ , and the time step is chosen such that  $\Delta t = h/4$  for  $k = 1$  and  $\Delta t = h$  for  $k = 2$ . For  $k = 3$  we use DIRK(3,4) and  $\Delta t = h$ .

Degree $k$	Mesh $1/h$	$\ \rho - \rho_h\ _{\mathcal{T}_h}$		$\ \rho \mathbf{u} - \rho \mathbf{u}_h\ _{\mathcal{T}_h}$		$\ E - E_h\ _{\mathcal{T}_h}$		$\ \mathbf{B} - \mathbf{B}_h\ _{\mathcal{T}_h}$		$\ \psi - \psi_h\ _{\mathcal{T}_h}$	
		Error	Order	Error	Order	Error	Order	Error	Order	Error	Order
1	8	3.31e-3	—	1.69e-2	—	2.21e-3	—	1.69e-2	—	2.26e-3	—
	16	4.22e-4	2.89	1.91e-3	3.15	4.22e-4	2.32	1.90e-3	3.15	4.89e-4	2.21
	32	8.42e-5	2.32	3.76e-4	2.34	9.83e-5	2.10	3.74e-4	2.34	1.17e-4	2.07
	64	1.97e-5	2.10	8.88e-5	2.08	2.41e-5	2.03	8.84e-5	2.08	2.88e-5	2.02
2	8	6.08e-3	—	1.03e-2	—	8.06e-4	—	1.02e-2	—	4.31e-4	—
	16	2.04e-3	1.57	1.52e-3	2.76	2.33e-4	1.79	1.47e-3	2.79	1.22e-4	1.83
	32	4.45e-4	2.20	2.05e-4	2.89	4.24e-5	2.45	1.92e-4	2.94	2.32e-5	2.39
	64	7.22e-5	2.63	2.73e-5	2.91	5.77e-6	2.88	2.46e-5	2.96	3.49e-6	2.73
	128	9.45e-6	2.93	3.61e-6	2.92	6.88e-7	3.07	3.13e-6	2.97	4.68e-7	2.90
3	8	4.87e-4	—	2.45e-2	—	2.85e-5	—	2.45e-2	—	1.53e-5	—
	16	4.08e-5	3.58	2.89e-3	3.08	1.87e-6	3.93	2.89e-3	3.08	1.08e-6	3.83
	32	2.17e-6	4.23	2.18e-4	3.73	1.20e-7	3.96	2.18e-4	3.73	7.17e-8	3.91
	64	8.78e-8	4.63	1.43e-5	3.93	8.14e-9	3.88	1.43e-5	3.93	4.60e-9	3.96
	128	3.54e-9	4.63	9.08e-7	3.98	5.38e-10	3.92	9.08e-7	3.98	2.90e-10	3.98

**Table 2**

Comparison between the numerical errors of the HDG scheme applied to Dedner's GLM-MHD [14] and Derigs' GLM-MHD [15] for the polarized Alfvén wave problem at  $T = 1$ . We have chosen  $k = 2$  and  $\Delta t = h$  with a DIRK(3,3) time integration scheme. The same trends hold for other polynomial orders.

Mesh $1/h$	$\ \rho - \rho_h\ _{\mathcal{T}_h}$		$\ \rho \mathbf{u} - \rho \mathbf{u}_h\ _{\mathcal{T}_h}$		$\ E - E_h\ _{\mathcal{T}_h}$		$\ \mathbf{B} - \mathbf{B}_h\ _{\mathcal{T}_h}$		$\ \psi - \psi_h\ _{\mathcal{T}_h}$	
	Dedner	Derigs	Dedner	Derigs	Dedner	Derigs	Dedner	Derigs	Dedner	Derigs
8	6.08e-3	5.30e-3	1.03e-2	1.03e-2	8.06e-4	6.57e-4	1.02e-2	1.02e-3	4.31e-4	3.61e-4
16	2.04e-3	1.95e-3	1.52e-3	1.51e-3	2.33e-4	1.84e-4	1.47e-3	1.47e-3	1.22e-4	1.04e-4
32	4.45e-4	4.14e-4	2.05e-4	2.02e-4	4.24e-5	3.30e-5	1.92e-4	1.91e-4	2.32e-5	1.88e-5
64	7.22e-5	6.56e-5	2.73e-5	2.61e-5	5.77e-6	4.62e-6	2.46e-5	2.44e-5	3.49e-6	2.69e-6
128	9.45e-6	8.29e-6	3.61e-6	3.24e-6	6.88e-7	5.97e-7	3.13e-6	3.09e-6	4.68e-7	3.51e-7

**Table 3**

Numerical errors in the divergence of the approximation to the magnetic induction for the smooth Alfvén waves problem. We set  $h = 1/16$  and  $\Delta t = h$  and we test two main configurations: no divergence cleaning and Derigs' GLM. For the GLM method we test the baseline and we also vary the propagation speed  $c_h$  and the damping source term  $\alpha$  to test their effect on the divergence errors.

$k$	No GLM		Derigs' GLM		$c_h \times 7$	
	$\ \nabla \cdot \mathbf{B}_h\ _{\mathcal{T}_h}$	$\sum_{F \in \mathcal{E}_h} \int_F  [\![\mathbf{B}_h]\!] $	$\ \nabla \cdot \mathbf{B}_h\ _{\mathcal{T}_h}$	$\sum_{F \in \mathcal{E}_h} \int_F  [\![\mathbf{B}_h]\!] $	$\ \nabla \cdot \mathbf{B}_h\ _{\mathcal{T}_h}$	$\sum_{F \in \mathcal{E}_h} \int_F  [\![\mathbf{B}_h]\!] $
1	1.2e-1	3.2e-2	1.1e-1	3.2e-2	3.5e-2	3.3e-2
2	1.3e-2	2.8e-3	6.6e-3	1.6e-3	1.2e-3	1.5e-3
3	1.7e-3	8.5e-5	6.6e-4	7.7e-5	1.5e-4	7.6e-5
4	1.4e-4	6.1e-6	2.3e-5	2.2e-6	4.1e-6	2.1e-6

$k$	$\alpha \times 5$		$\alpha/5$		$c_h \times 20$	
	$\ \nabla \cdot \mathbf{B}_h\ _{\mathcal{T}_h}$	$\sum_{F \in \mathcal{E}_h} \int_F  [\![\mathbf{B}_h]\!] $	$\ \nabla \cdot \mathbf{B}_h\ _{\mathcal{T}_h}$	$\sum_{F \in \mathcal{E}_h} \int_F  [\![\mathbf{B}_h]\!] $	$\ \nabla \cdot \mathbf{B}_h\ _{\mathcal{T}_h}$	$\sum_{F \in \mathcal{E}_h} \int_F  [\![\mathbf{B}_h]\!] $
1	1.1e-1	3.2e-2	1.1e-1	3.2e-2	8.5e-3	3.3e-2
2	6.3e-3	1.6e-3	6.7e-3	1.6e-3	8.2e-4	1.4e-3
3	6.6e-4	7.7e-5	6.6e-4	7.7e-5	3.6e-5	7.8e-5
4	2.3e-5	2.2e-6	2.3e-5	2.2e-6	2.1e-6	1.7e-6

from a Harris current sheet and featuring the development of magnetic islands and potentially secondary magnetic islands (plasmoids). The Harris current sheet can be viewed as a resistive boundary layer for the Alfvén wave velocity, and the Sweet-Parker scaling (laminar boundary layer theory) gives that the reconnection rate scales with  $\delta/L$ , and  $\delta/L \sim 1/\sqrt{S_r}$  (where  $\delta$  is the boundary layer half-width and  $L$  its half-length) [55]. The results using resistive MHD and the Sweet-Parker scaling are, however, orders of magnitude off from what happens in solar flares. These differences are attributed to the effect of whistler waves which are captured using Hall MHD model but not the MHD resistive model [5].

The setup for this problem consists of the domain  $\Omega = [-L_x/2, L_x/2] \times [-L_y/2, L_y/2]$ , where  $L_x = 25.6$  and  $L_y = 12.8$  with perfectly left and right walls, and perfectly conducting top and bottom walls. The boundary conditions associated with the perfectly conducting walls represent a mix of Dirichlet conditions  $u_y = B_y = 0$  and Neumann conditions  $\partial \rho / \partial y = \partial E / \partial y = \partial \psi / \partial y = \partial u_x / \partial y = \partial B_x / \partial y = 0$ . The initial velocity field is zero everywhere, as well as the  $y$  component of the magnetic induction. Also,  $\rho = \text{sech}^2(y/l) + 0.2$ ,  $B_x = B_0 \tanh(y/l)$  and  $p = c B_0^2 \rho / 2$  where  $B_0 = 1$  and  $l = 0.5$ . The magnetic field is perturbed by

**Table 4**

History of numerical errors and convergence orders for the HDG, IEDG and EDG formulations for the magnetic vortex problem after one period at  $T = 10$ . Time integration is carried out using a DIRK(2,2) for  $k = 1$ , DIRK(3,3) for  $k = 2$  and DIRK(3,4) scheme for  $k = 3$ , and the time step is chosen such that  $\Delta t = h$ . All runs use quadrilateral elements. We show the magnetic induction.

Mesh $1/h$	Scheme	$k = 1$		$k = 2$		$k = 3$	
		$\ \mathbf{B} - \mathbf{B}_h\ _{\mathcal{T}_h}$	Order	$\ \mathbf{B} - \mathbf{B}_h\ _{\mathcal{T}_h}$	Order	$\ \mathbf{B} - \mathbf{B}_h\ _{\mathcal{T}_h}$	Order
8	HDG	2.68e-1	—	7.81e-2	—	5.07e-2	—
	IEDG	2.61e-1	—	7.59e-2	—	5.11e-2	—
	EDG	2.91e-1	—	7.56e-2	—	5.11e-2	—
16	HDG	7.85e-2	1.77	1.13e-2	2.79	3.97e-3	3.67
	IEDG	7.85e-2	1.73	1.11e-2	2.77	4.00e-3	3.68
	EDG	1.78e-1	0.71	1.11e-2	2.77	4.00e-3	3.68
32	HDG	8.47e-3	3.21	1.25e-3	3.18	2.45e-4	4.02
	IEDG	7.56e-3	3.38	1.26e-3	3.14	2.44e-4	4.04
	EDG	2.84e-2	2.65	1.26e-3	3.14	2.44e-4	4.04
64	HDG	9.90e-4	3.10	1.52e-4	3.04	1.59e-5	3.95
	IEDG	8.49e-4	3.15	1.56e-4	3.01	1.58e-5	3.95
	EDG	2.78e-3	3.35	1.53e-4	3.04	1.58e-5	3.95

$$B'_x = \psi_0 \frac{\pi}{L_y} \sin\left(\frac{\pi y}{L_y}\right) \cos\left(\frac{2\pi x}{L_x}\right)$$

and

$$B'_y = \psi_0 \frac{2\pi}{L_x} \sin\left(\frac{2\pi x}{L_x}\right) \cos\left(\frac{\pi y}{L_y}\right)$$

with  $\psi_0 = 0.1$ . Results for this problem using resistive MHD can be found in [6,43].

We use an unstructured mesh consisting of 11348 triangular elements and the HDG scheme with  $k = 5$ . We show the mesh and the initial conditions in Fig. 1. We notice how the initial perturbation causes the magnetic field lines to pinch the Harris current sheet. Firstly, we set  $\eta_f = 8e-3$  and we look at the effect of our physics-based shock capturing on under-resolved problems. We note that as the simulation progresses the current sheet gets smaller and thinner until reconnection occurs, and as such, one would reach a time when its thickness will be beyond computational resolution. For example, using a  $64 \times 32$  quadrilateral mesh with  $k = 2$ , at  $t = 86$  the under-resolution related oscillations will lead to negative pressures and simulation blowup, while using shock capturing enables us to run until  $t_{\text{final}} = 200$  without any problem. For the mesh shown in Fig. 1 with  $k = 5$  we do not require shock capturing to run until the final time, however, under-resolution causes oscillations at  $t = 100$  as shown in Fig. 2. We can clearly see that we add enough artificial resistivity to remove spurious oscillations without negatively affecting the numerical solution.

In Fig. 3, we show the development of the problem for three values of  $\eta_f$  with  $k = 5$ . As  $\eta_f$  decreases we notice that the magnetic islands also decrease and the width of the current sheet decreases, while its length increases (consistent with the Sweet-Parker scaling, given the increase in  $S_r$ ). For  $\eta_f = 8e-3$  and  $\eta_f = 5e-3$  the solution is symmetric, well resolved and oscillation free. For  $\eta_f = 1e-3$  the resistive Lundquist number is high enough such that magnetic reconnection is replaced by a plasma tearing instability (as also observed in [6]) which leads to the formation of secondary magnetic islands, or plasmoids (last image in Fig. 3). In this case, our shock capturing mechanism fails to completely remove spurious oscillations, which, together with the mesh anisotropy, destroy the symmetry of the solution. This suggests that there are improvements to be made in our shock capturing method for high  $k$  and plasma tearing instabilities. (If using  $k = 1, 2$  and the same mesh no loss of symmetry is observed but numerical diffusion suppresses the physical instability).

Finally, in Table 5 we show that for resistive MHD flows the block ILU0 (incomplete LU factorization with zero fill-in) preconditioner introduced in [20] is effective at keeping the problem well-conditioned for both HDG and IEDG and for various meshes and polynomial orders. We see that the number of GMRES iterations increases slightly as we increase  $k$  and/or reduce  $h$ . The number of GMRES iterations for IEDG is smaller than that for HDG since IEDG has less globally coupled unknowns than HDG. For all cases, the number of Newton iterations required to obtain the norm of the residual to an error of  $10^{-8}$  varies from 2 to 3 for  $\Delta t = 0.1$  depending on the polynomial degree  $k$  and the mesh used. For each Newton iteration, the overall cost includes the local solves (namely, static condensation), the factorization of the block ILU0 preconditioner, and the global linear solve. The factorization of the block ILU0 preconditioner often takes less than 10% of the overall cost since it is done once and reused. The computational cost of the local solves ranges from 30% to 50% of the overall cost: (i) the local solves are just as expensive as the global linear solve for IEDG, whereas they are less expensive than the global linear solve for HDG; (ii) using higher polynomial degree  $k$  will lead to higher percentage of the cost of the local solves. The computational cost of applying the block ILU0 preconditioner takes about 40% of the global linear solve. It

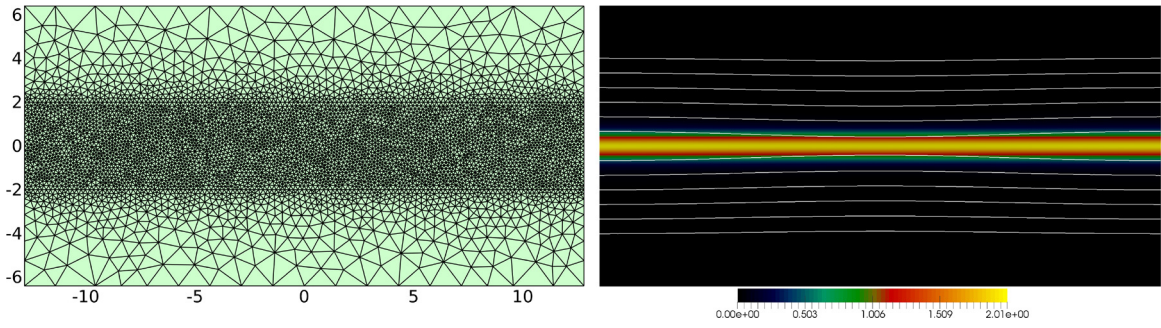


**Fig. 1.** Mesh and initial conditions for the GEM Reconnection problem. The colour map shows the out-of-plane component of the current density,  $J_z$ , while the white lines are magnetic field lines seeded from the left wall.

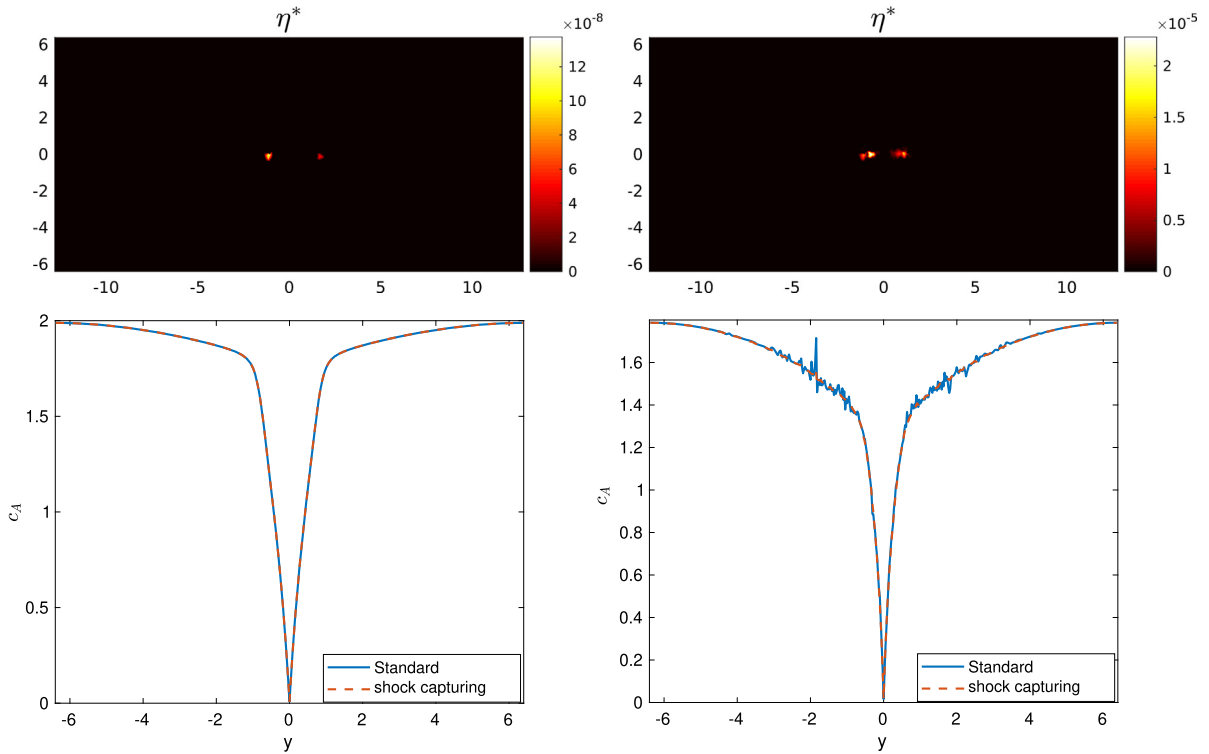


**Fig. 2.** The effect of shock capturing on the solution of the GEM Reconnection challenge with  $\eta_f = 8e-3$  at  $t = 50$  (left) and  $t = 100$  (right).

should be mentioned that, without the block ILU0 preconditioner, GMRES does not converge to the specified tolerance even for 1000 iterations, eventually causing the simulation to blow up.

#### 5.4. Orszag-Tang vortex

The Orszag-Tang vortex was initially proposed as a test case to study 2D MHD turbulence [49,13,52] and was later adopted by the numerical analysis community as the validation case for MHD shock capturing due to its complex shock pattern [14,15,2,40,36,30,56]. We use this problem since it allows us to test transition to supersonic MHD turbulence, the formation of shocks, shock-shock interactions, plasma tearing instabilities and the effect of divergence cleaning.

We adopt the same ideal MHD setup as presented in [56], where  $\Omega = [0, 1]^2$  with periodic boundary conditions. The initial conditions are smooth with  $\gamma = 5/3$ ,  $\rho = 25/36\pi$  and  $p = 5/12\pi$  (this gives  $a^2 = 1$ ). The initial velocities are periodic:  $u_x = -\sin(2\pi y)$ ,  $u_y = \sin(2\pi x)$  and the initial magnetic field is also periodic:  $B_x = -B_0 \sin(2\pi y)$ ,  $B_y = B_0 \sin(4\pi x)$ , with  $B_0 = 1/\sqrt{4\pi}$  (the initial conditions trivially satisfy  $\nabla \cdot \mathbf{B} = 0$ ).

For the solution of this problem, we use the HDG scheme with  $k = 6$  and a grid of  $128 \times 128$  quadrilaterals in order to demonstrate the robustness of our shock capturing for high-order discretization. In Fig. 4, we compare our results against those obtained using Athena in [56] and a  $512 \times 512$  grid. Athena is an open source 3rd order reconstruction finite vol-

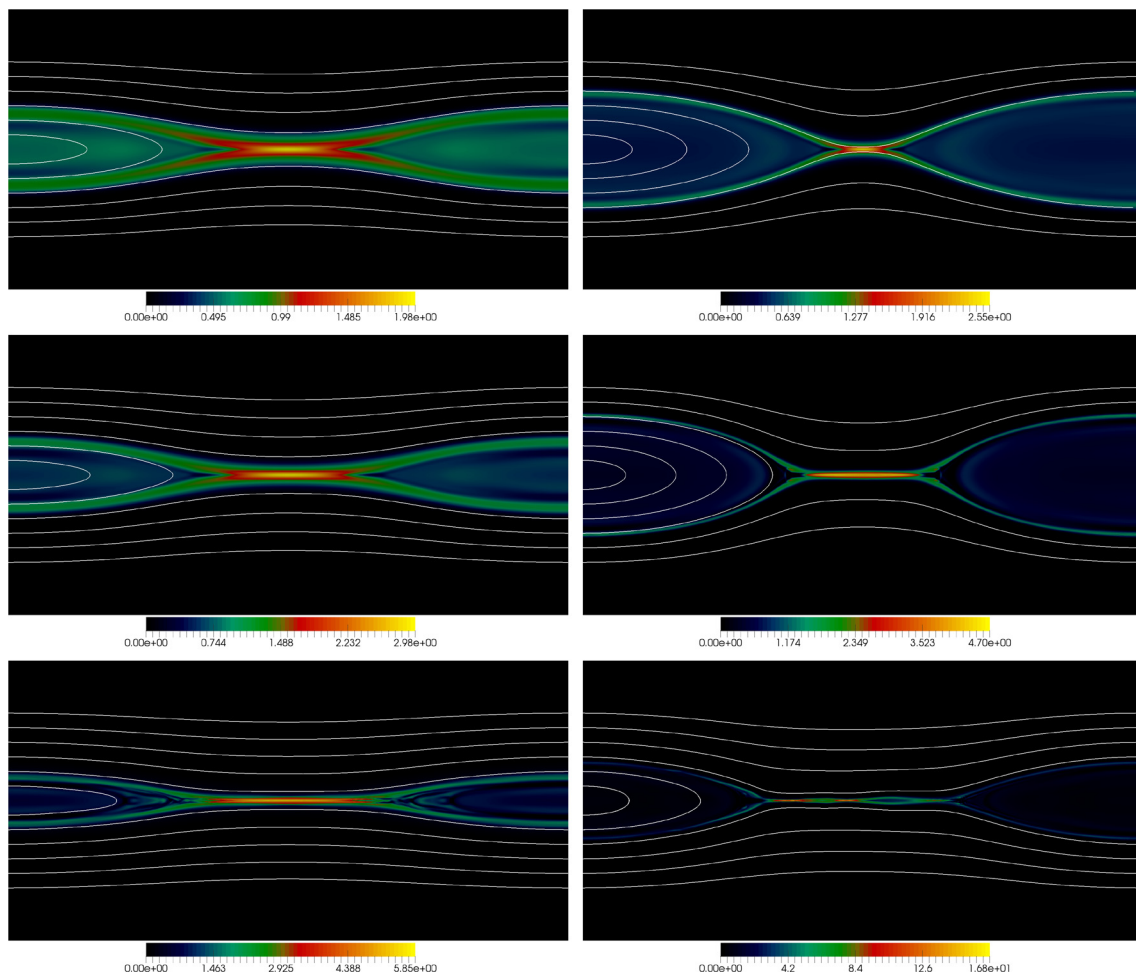


**Fig. 3.** Evolution of the GEM Reconnection problem for various values of  $\eta_f$ :  $8e-3$  (top),  $5e-3$  (middle) and  $1e-3$  (bottom). On the left we show the solution at  $t = 50$  and on the right at  $t = 100$ . The colour map shows  $J_z$  and the white lines are magnetic field lines seeded from the left wall.

**Table 5**

The number of GMRES iterations needed to converge the linear residual to a value of  $10^{-13}$  for each non-linear Newton iteration, for  $\Delta t = 0.1$ . The value of resistivity associated with the Lundquist number shown is  $\eta_f = 8e-2$ . We show results for simple, structured quadrilateral meshes, as well as the unstructured mesh shown in Fig. 1.

Lundquist number	Mesh	Scheme	$k = 1$	$k = 2$	$k = 3$	$k = 4$
$S_r = 160$	$64 \times 32$	HDG	16	25	30	38
		IEDG	14	18	23	27
	$128 \times 64$	HDG	23	35	43	55
		IEDG	19	28	33	38
	Unstructured	HDG	24	32	41	52

ume solver using constrained transport reconstruction to enforce the solenoidal involution (5). We can see that the results match extremely well, suggesting that our shock capturing method gives very sharp smooth shock profiles, and that using a Lax Friedrich solver with high order polynomial approximations allows us to capture all the relevant waves for this problem. In Fig. 5 we track the evolution of the solution. Shocks quickly develop from the smooth initial conditions and start interacting. The interaction of 4 shocks leads to the formation of a central current sheet. This current sheet undergoes a tearing instability which leads to the formation of plasmoids which move along the current sheet, coalesce and eventually die away. We can notice two other current sheets on the left and right, which in turn develop plasmoids. It is easy to see that as the simulation progresses the solution becomes more and more chaotic, exhibiting enhanced mixing and transition to turbulence.

We report the evolution of the divergence errors in Table 6. When we use no divergence cleaning the errors quickly grow to very large values and they cause the Newton solver to stop converging at  $t \approx 0.3125$ . Using the GLM approach

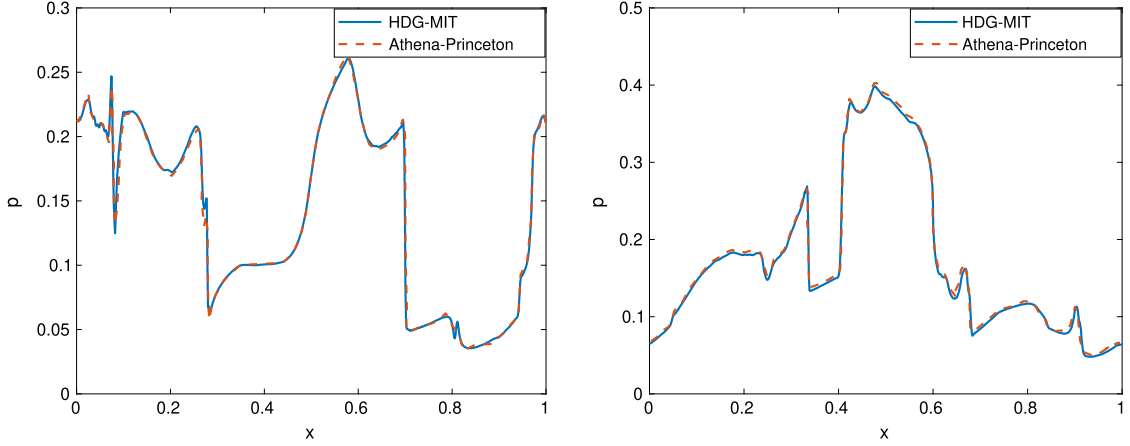


**Fig. 4.** Comparison between the HDG scheme presented here and the Athena solver [56] for the Orszag-Tang vortex at  $t = 0.5$ . We show slices of dimensionless pressure at  $y = 0.3125$  (left) and  $y = 0.4277$  (right).

**Table 6**

Numerical errors in the divergence of the approximation to the magnetic induction for the Orszag-Tang vortex. We test three configurations: no divergence cleaning, Derigs' GLM and Derigs' GLM with seven times the propagation speed. The  $\times$  mark symbolizes that the simulation failed to converge.

$t$	No GLM		Derigs' GLM		$c_h \times 7$	
	$\ \nabla \cdot B_h\ _{\mathcal{T}_h}$	$\sum_{F \in \mathcal{E}_h} \int_F \llbracket B_h \rrbracket$	$\ \nabla \cdot B_h\ _{\mathcal{T}_h}$	$\sum_{F \in \mathcal{E}_h} \int_F \llbracket B_h \rrbracket$	$\ \nabla \cdot B_h\ _{\mathcal{T}_h}$	$\sum_{F \in \mathcal{E}_h} \int_F \llbracket B_h \rrbracket$
0.1	$2.9e-1$	$5.3e-5$	$2.9e-3$	$3.7e-5$	$4.5e-4$	$7.4e-5$
0.2	6.5	$5.7e-4$	$2.8e-1$	$7.8e-4$	$4.4e-2$	$1.9e-3$
0.3	31.2	$4.0e-3$	$3.9e-1$	$2.5e-3$	$6.1e-2$	$5.4e-3$
0.4	$\times$	$\times$	$4.2e-1$	$3.8e-3$	$8.2e-2$	$9.8e-3$
0.5	$\times$	$\times$	$6.0e-1$	$4.6e-3$	$1.0e-1$	$1.1e-2$

keeps the errors in check, while increasing  $c_h$  by a factor of 7 reduces the error in the  $L^2$  norm by one order of magnitude and increases the cumulative error in the normal jump across faces by one order of magnitude. This seems a reasonable compromise, given that the dominant component of the error is in the  $L^2$  norm. Finally, in Fig. 6, we show the two sensors  $\hat{s}_\beta$  and  $\hat{s}_\eta$ . While at  $t = 0.234$  both sensors capture the shocks, at  $t = 0.488$ ,  $\hat{s}_\eta$  does not capture properly the weak shocks, while  $\hat{s}_\beta$  does. Our approach of blending the two is then warranted, since  $\hat{s}_\beta$  does not capture the under-resolved current sheet, while  $\hat{s}_\eta$  does. We also note that we add sufficient resistivity to stabilize the current sheet, while not inhibiting the formation of plasmoids, which is a well-known issue for overly-dissipative  $\eta^*$  formulations [59].

### 5.5. MHD rotor

The MHD Rotor problem was initially proposed by Balsara and Spicer [2] as a means to test MHD shock capturing and the treatment of the divergence free condition (5), since no divergence treatment can lead to large shock oscillations and overshoots, see e.g. [60]. From a physics point of view, this problem tests the propagation of strong torsional Alfvén waves and is relevant for star formation [2]. The initial conditions feature a dense rotating disk in a quiescent ambient medium, which, due to the imbalance caused by the centrifugal force, starts launching torsional Alfvén waves. These waves lead to the build-up of magnetic pressure around the disk, which turns the circular disk into an oval as time progresses.

We set up the problem following [60] to facilitate comparison with their results:  $\Omega = [0, 1]^2$  with periodic boundary conditions. The initial conditions are given by:  $\gamma = 5/3$ ,  $p = 0.5$ ,  $B_y = 0$  and  $B_x = 2.5/(4\pi)$ . Density and velocity are given by:

$$\rho = \begin{cases} 10, & r \leq r_0 \\ 1 + 9f(r), & r_0 < r < r_1 \\ 1, & r_1 \leq r \end{cases}$$

$$u_x = \begin{cases} -(y - 0.5)/r_0, & r \leq r_0 \\ -f(r)(y - 0.5)/r, & r_0 < r < r_1 \\ 0, & r_1 \leq r \end{cases}$$

$$u_y = \begin{cases} (x - 0.5)/r_0, & r \leq r_0 \\ f(r)(x - 0.5)/r, & r_0 < r < r_1 \\ 0, & r_1 \leq r \end{cases}$$

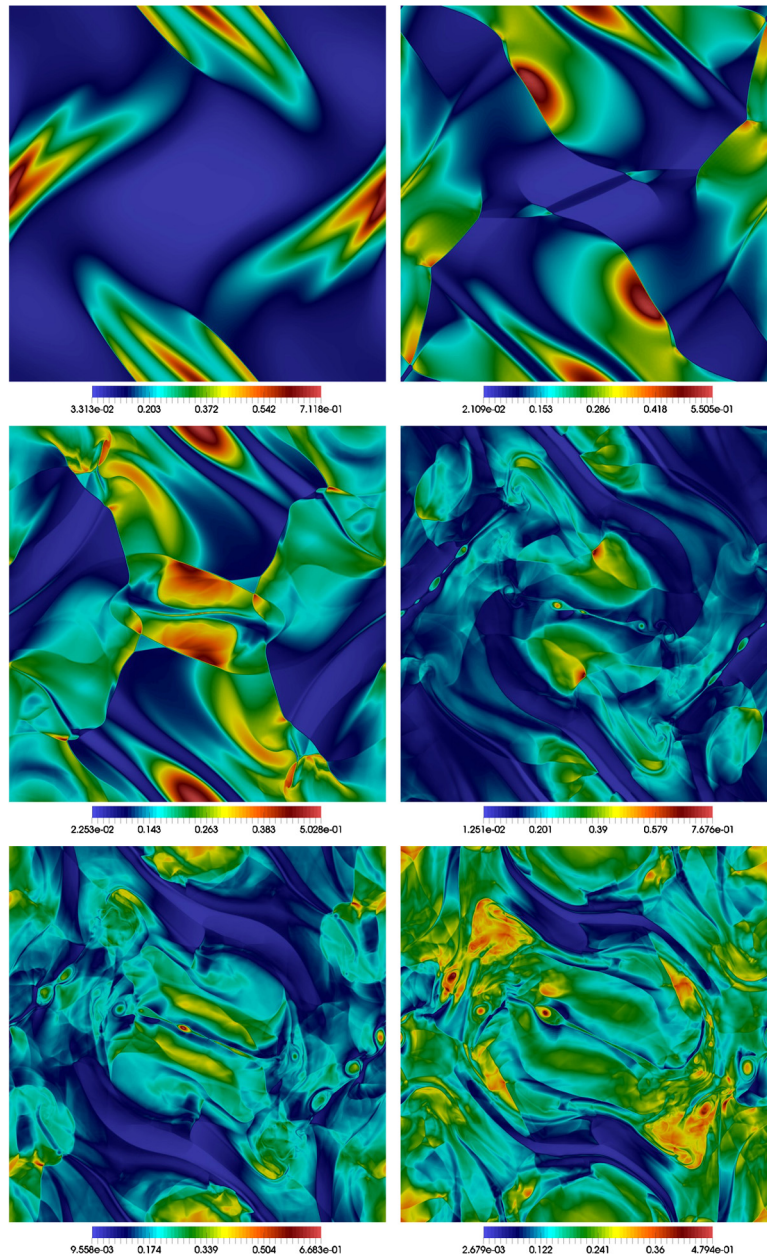


**Fig. 5.** Evolution of the Orszag-Tang Vortex problem. We show pressure at times (from top to bottom, left to right)  $t = 0.176$ ,  $t = 0.352$ ,  $t = 0.508$ ,  $t = 0.629$ ,  $t = 0.879$  and  $t = 1$ .

where  $r = \sqrt{(x - 0.5)^2 + (y - 0.5)^2}$ ,  $r_0 = 0.1$ ,  $f(r) = (r_1 - r) / (r_1 - r_0)$  and  $r_1 = 0.115$ .

For the solution of this problem, we use a grid of  $128 \times 128$  quadrilaterals with  $k = 6$  in order to demonstrate the robustness of our shock capturing for high-order discretization. In Fig. 7, we compare our results against data presented in [60] where an explicit TVD Central Discontinuous Galerkin (CDG) method is used with  $k = 2$  and a  $600 \times 600$  grid. We can notice that the shocks are sharp and non-oscillatory, in spite of the high  $k$  and coarse mesh. Moreover, we can notice that there are no differences between HDG, IEDG and EDG. We also observe that our results match well without overshoots, suggesting that our shock capturing is robust. To further support this argument we present Fig. 8 and Table 7. We can notice in Fig. 8 that the errors are concentrated around the shocks. This is expected, and has been extensively illustrated in the literature, for various problems [58]. We also note in Table 7 that using divergence cleaning the error is reduced by a factor of 12 at  $t = 0.1475$ . In fact, the nonlinear solver fails to converge at around  $t = 0.2$  without divergence cleaning. Similarly to the Orszag-Tang vortex, we notice that increasing  $c_h$  leads to reducing the  $L^2$  error, but accumulates errors at element faces.

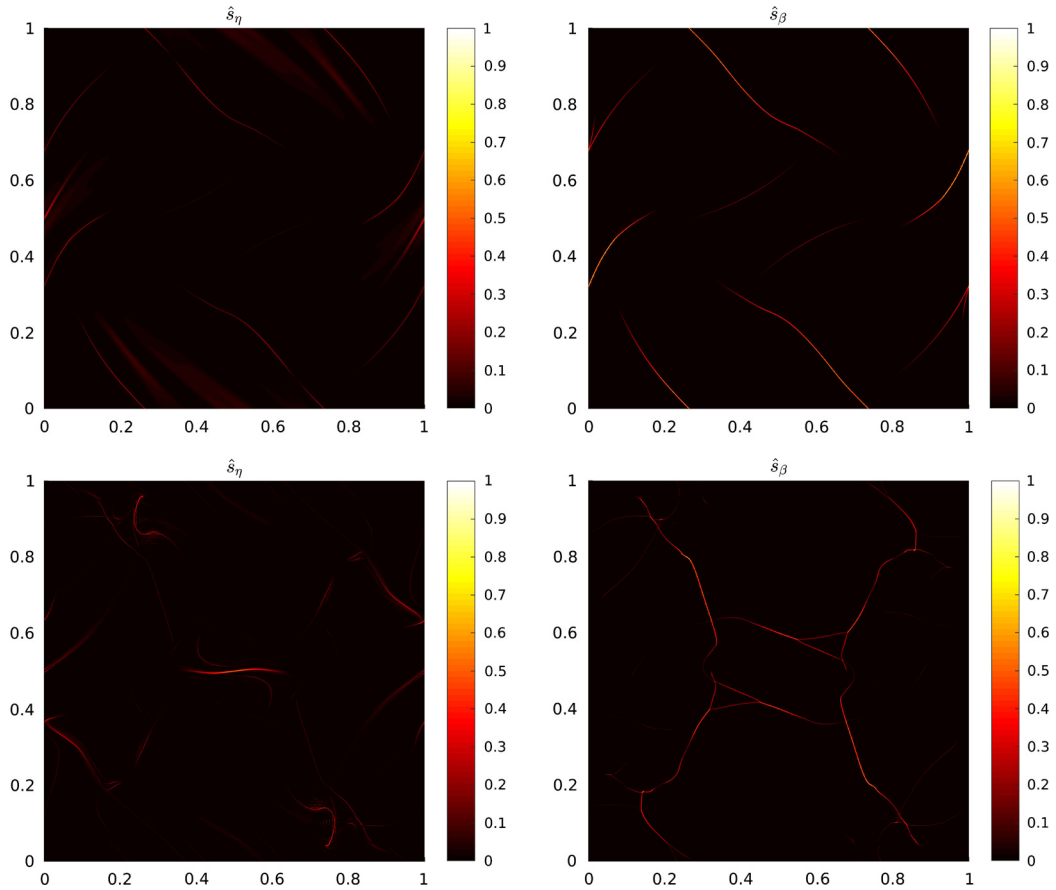


Fig. 6. Artificial resistivity and artificial bulk viscosity sensors at  $t = 0.234$  (top) and  $t = 0.488$  bottom.

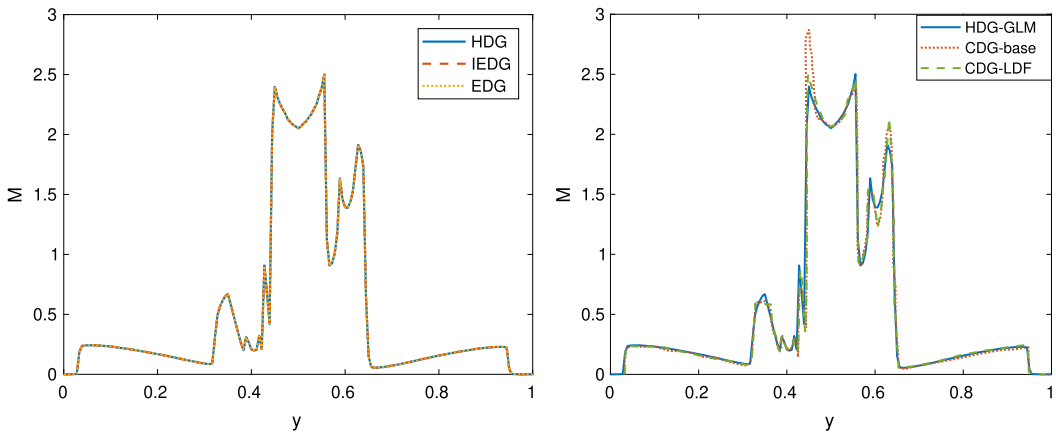


Fig. 7. Comparison between the HDG, IEDG and EDG solutions on the left, and our solution and the results presented in [60] on the right, for the MHD Rotor problem. We take a slice at  $x = 0.413$  and  $t = 0.295$  and we show the Mach number. In the legend, *base* indicates no magnetic divergence treatment, while LDF indicates locally divergence free basis for the polynomial approximation of  $\mathbf{B}$ .

Increasing  $c_h$  by a factor of 7 reduces the error by a factor of 2.5, and increasing  $c_h$  by a factor of 20 reduces the error by a factor of 4. However, we run into convergence issues when the value of  $c_h$  is too high, suggesting that perhaps the best option for  $c_h$  is not a constant, but rather a function of the local solution. We notice no visible improvements by varying  $\alpha$ , which is consistent with Derigs' [15] observation about the effect of the that the boundary conditions on the best choice for  $\alpha$ .

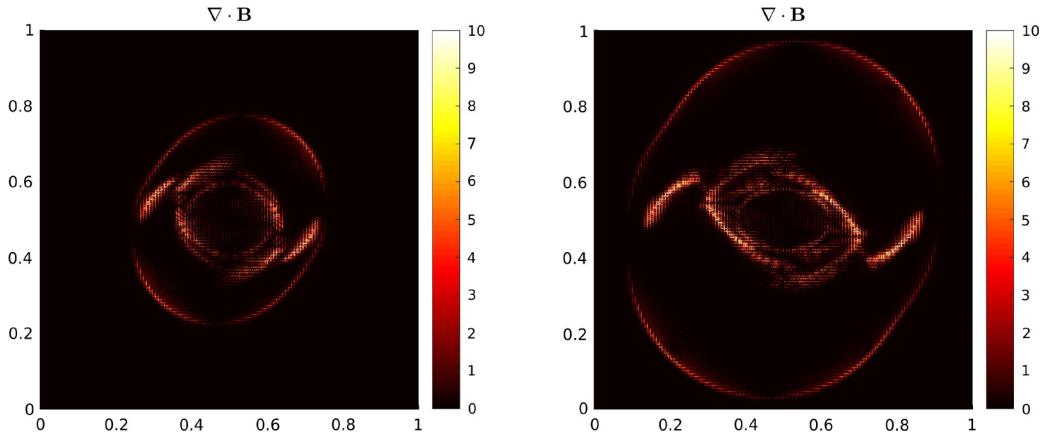


Fig. 8. Divergence errors for the MHD Rotor problem at  $t = 0.1475$  (left) and  $t = 0.295$  (right).

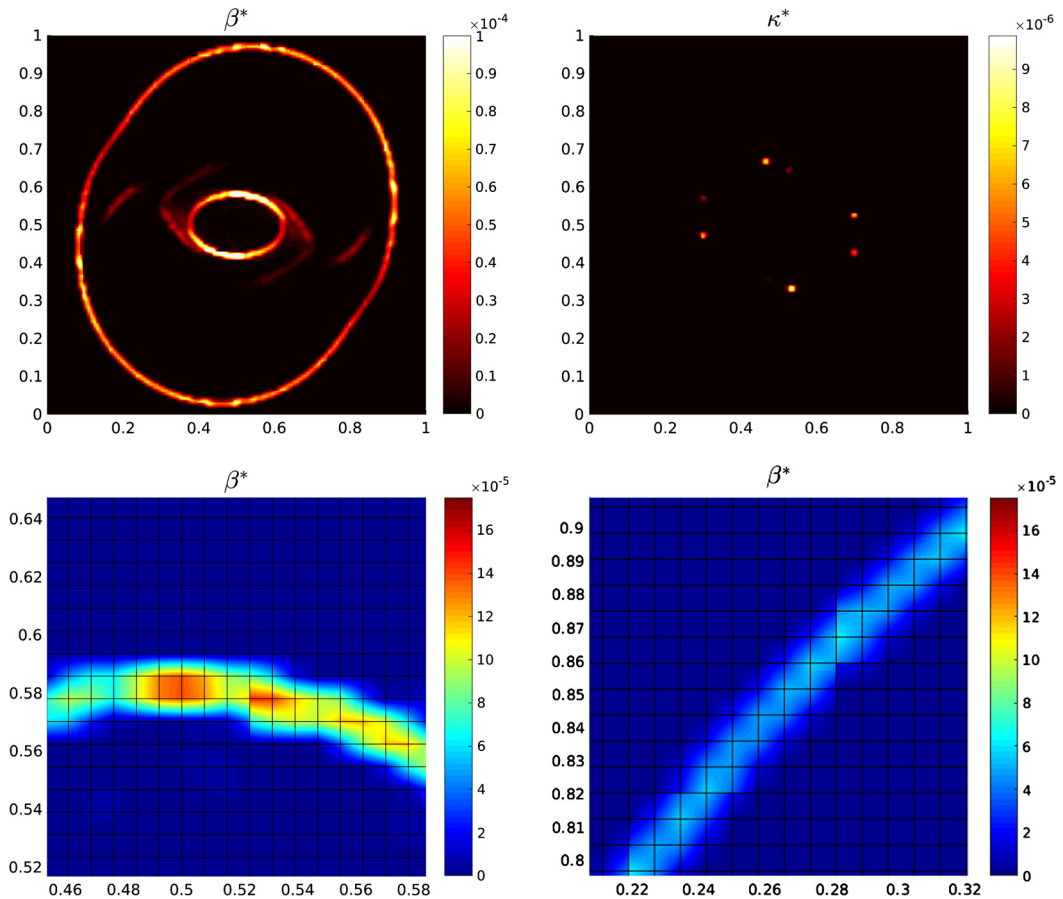


Fig. 9. Artificial bulk viscosity and artificial thermal conductivity for the MHD Rotor problem at  $t = 0.295$  on top. On the bottom we zoom in on a strong shock (left) and a weak shock (right) both misaligned with respect to the grid, and show the artificial bulk viscosity.

In Fig. 9, we show  $\beta^*$  and  $\kappa^*$  at  $t = 0.295$ . We notice that we are adding  $\kappa^*$  only for a few troubled elements, which see larger gradients in  $T$ , but its magnitude is small nonetheless (also  $\mu^* = 0$ ). We can also notice that the artificial bulk viscosity is able to detect all shocks and resolve them irrespective of their grid alignment, however  $\beta^*$  is smeared over 2-3 elements. This could potentially be improved through a better smoothing operator, such as a truncated Gaussian filter, but this was not investigated here. Finally, we visualize the development of the solution at  $t = 0.1475$  and  $t = 0.295$  in Fig. 10, for the HDG solution. The results compare very well qualitatively with other results from literature [2,60].

**Table 7**

Comparison of the divergence errors for the MHD Rotor problem with and without the Lagrange multiplier. For the Lagrange multiplier approach we also vary the parameters and note their effect. The × mark symbolises that the simulation crashed, or failed to converge.

	$t = 0.1475$		$t = 0.295$	
	$\ \nabla \cdot B_h\ _{\mathcal{T}_h}$	$\sum_{F \in \mathcal{E}_h} \int_F  [[B_h]] $	$\ \nabla \cdot B_h\ _{\mathcal{T}_h}$	$\sum_{F \in \mathcal{E}_h} \int_F  [[B_h]] $
No GLM	10.02	5.6e−4	×	×
Derigs' GLM	0.82	3.0e−3	1.31	5.8e−3
$c_h \times 7$	0.35	4.3e−3	0.52	6.6e−3
$c_h \times 20$	0.21	3.8e−3	×	×
$\alpha \times 5$	0.80	3.0e−3	1.31	5.8e−3
$\alpha/5$	0.82	3.0e−3	1.31	5.8e−3

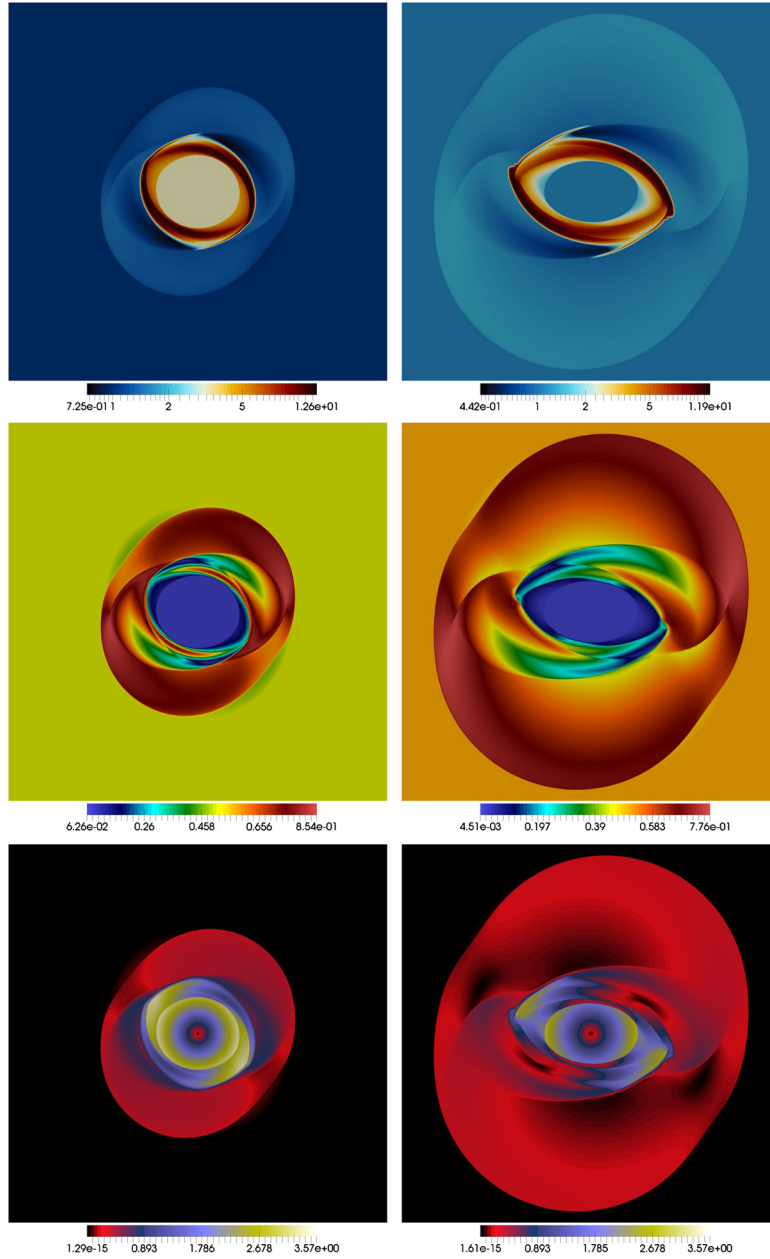


**Fig. 10.** Evolution of the MHD Rotor problem at  $t = 0.1475$  (left) and  $t = 0.295$  (right). We show density (first row), pressure (second row) and Mach number (third row).

## 6. Concluding remarks

We have presented a class of implicit hybridized DG methods for ideal and resistive magnetohydrodynamics using a generalized Lagrange multiplier approach to control the error in the divergence of the magnetic field. We have also proposed a physics-based artificial viscosity shock capturing method for MHD problems. Below, we summarize the main results of this paper.

We have validated our numerical scheme for smooth, ideal MHD problems with known analytic solutions. The HDG, EDG and IEDG methods converge at the optimal rate of  $k+1$  for all conserved variables. IEDG appears as the best option in terms of both efficiency and accuracy. We compared two Lagrange multiplier approaches for divergence cleaning, Dedner's [14] and Derigs' [15] and we have found Derigs' method to give consistently better results. We also have investigated the effect of divergence cleaning for smooth problems and found that even if no divergence cleaning was employed, our method was stable and the divergence errors decreased with increasing polynomial order. However, using Derigs' GLM method resulted in errors which were one order of magnitude smaller. We have found that varying the damping source term  $\alpha$  did not have visible effects, while varying  $c_h$  has significant effects on both the divergence error and the conditioning of the system.

We have tested our scheme to handle resistive MHD through the GEM magnetic reconnection problem. Our results matched well qualitatively with those obtained by other authors and followed the expected trends of the Sweet-Parker scaling. We have also tested our solver for resistive MHD flows and found it well-suited, giving well-conditioned systems for both HDG and IEDG, irrespective of the polynomial order, or irrespective of whether the mesh was structured and formed of quadrilaterals, or unstructured, and formed of triangular elements. We have also studied the effect of our artificial resistivity for under-resolved problems and found it to remove spurious oscillations, while not altering the physics of the problem. However, when lowering the physical resistivity to the extent that the reconnection phenomenon was replaced by a plasma tearing instability, our artificial resistivity recipe was no longer enough to stabilize the problem in a highly under-resolved regime.

Finally, we have demonstrated our shock capturing method for two non-smooth problems, namely, the Orszag-Tang vortex and the MHD rotor. Our numerical solutions yielded very sharp shock profiles without oscillations even if we used coarse meshes and high polynomial orders. Moreover, our results matched well against other well-established MHD solvers. As far as shock-sensing is concerned, we observed that the sensor for the artificial bulk viscosity was able to detect and stabilize shocks. However, this was not always the case for our artificial resistivity sensor, which was still of paramount importance for features such as under-resolved current sheets. For shock dominated problems, not using any divergence cleaning quickly resulted in large errors and spurious oscillations which caused the solver to crash. Increasing  $c_h$  to large extents, as we did for smooth problems, was no longer universally better, since it reduced the errors in the  $L^2$  norm, but resulted in the accumulation of errors at the element faces.

Future work should investigate the following two areas: developing divergence-free HDG methods that yield a divergence-free approximation to the magnetic field, and entropy-stable HDG methods that produce entropy-satisfying approximate solutions.

### Declaration of competing interest

The authors declare that they have no known competing financial interests or personal relationships that could have appeared to influence the work reported in this paper.

### Acknowledgements

The authors acknowledge Pratt & Whitney, the Air Force Office of Scientific Research (FA9550-16-1-0214) and the National Aeronautics and Space Administration (NASA NNX16AP15A) for supporting this work. C. Ciucă would like to thank Dr. Oliver R.H. Buxton of Imperial College for his comments and suggestions that have helped shape the work presented here. P. Fernandez acknowledges the financial support from the Zakhartchenko Fellowship.

### References

- [1] H. Abbassi, F. Mashayek, G.B. Jacobs, Shock capturing with entropy-based artificial viscosity for staggered grid discontinuous spectral element method, *Comput. Fluids* 98 (2014) 152–163.
- [2] D.S. Balsara, D.S. Spicer, A staggered mesh algorithm using high order Godunov fluxes to ensure solenoidal magnetic fields in magnetohydrodynamic simulations, *J. Comput. Phys.* 149 (1999) 270.
- [3] G.E. Barter, D.L. Darmofal, Shock capturing with PDE-based artificial viscosity for DGFEM: Part I. Formulation, *J. Comput. Phys.* 229 (5) (2010) 1810–1827.
- [4] T. Barth, On the role of involutions in the discontinuous Galerkin discretization of Maxwell and magnetohydrodynamic systems, in: Shashkov Arnold Boshev (Ed.), *IMA Volume on Compatible Discretizations*, Springer-Verlag, 2005.
- [5] J. Birn, J.F. Drake, M.A. Shay, B.N. Rogers, R.E. Denton, M. Hesse, M. Kuznetsova, Z.W. Ma, A. Bhattacharjee, A. Otto, P.L. Pritchett, Geospace environmental modeling (GEM) magnetic reconnection challenge, *J. Geophys. Res.* 106 (2001) 3715–3719.
- [6] J. Birn, M. Hesse, Geospace environmental modeling (GEM) magnetic reconnection challenge: resistive tearing, anisotropic pressure and Hall effects, *J. Geophys. Res.* 106 (2001) 3737–3750.
- [7] D. Biskamp, *Nonlinear Magnetohydrodynamics*, Cambridge Monographs on Plasma Physics, Cambridge University Press, 1993.

- [8] J.U. Brackbill, D.C. Barnes, The effect of nonzero  $\nabla \cdot \mathbf{B}$  on the numerical solution of magnetohydrodynamic equations, *J. Comput. Phys.* 35 (1980) 426.
- [9] B. Cockburn, Discontinuous Galerkin methods for computational fluid dynamics, in: Erwin Stein, et al. (Eds.), *Encyclopedia of Computational Mechanics*, in: *Fluids*, vol. 3, Wiley Library, 2014, pp. 90–130, chapter 4.
- [10] B. Cockburn, J. Gopalakrishnan, R. Lazarov, Unified hybridization of discontinuous Galerkin, mixed and continuous Galerkin methods for second order elliptic problems, *SIAM J. Numer. Anal.* 47 (2009) 1319–1365.
- [11] A.W. Cook, W.H. Cabot, Hyperviscosity for shock-turbulence interactions, *J. Comput. Phys.* 195 (2004) 594–601.
- [12] A.W. Cook, W.H. Cabot, A high-wavenumber viscosity for high resolution numerical method, *J. Comput. Phys.* 203 (2005) 379–385.
- [13] R.B. Dahlburg, J.M. Picone, Evolution of the Orszag–Tang vortex system in a compressible medium. I. Initial average subsonic flow, *Phys. Fluids, B Plasma Phys.* 1 (11) (1989) 2153–2171.
- [14] A. Dedner, F. Kemm, D. Kröner, C.-D. Munz, T. Schnitzer, M. Wesenberg, Hyperbolic divergence cleaning for the MHD equations, *J. Comput. Phys.* 175 (2002) 645–673.
- [15] D. Derigs, A.R. Winters, G.J. Gassner, S. Walch, M. Böhm, Ideal GLM-MHD: about the entropy consistent nine-wave magnetic field divergence diminishing ideal magnetohydrodynamics equations, *J. Comput. Phys.* 364 (2018) 420–467.
- [16] S. Dorch, F. Bertil, *Magnetohydrodynamics, Scholarpedia* 2 (4) (2007) 2295, revision #91454.
- [17] M. Dumbser, D.S. Balsara, E.F. Toro, C.-D. Munz, A unified framework for the construction of one-step finite-volume and discontinuous Galerkin schemes on unstructured meshes, *J. Comput. Phys.* 227 (2008) 8209–8253.
- [18] P. Fernandez, Entropy-Stable Hybridized Discontinuous Galerkin Methods for Large-Eddy Simulation of Transitional and Turbulent Flows, PhD thesis, Department of Aeronautics and Astronautics, Massachusetts Institute of Technology, 2019.
- [19] P. Fernandez, N.C. Nguyen, J. Peraire, A physics-based shock capturing method for large-eddy simulations. Under review, arXiv preprint, arXiv:1806.06449, 2018.
- [20] P. Fernandez, N.C. Nguyen, J. Peraire, The hybridized discontinuous Galerkin method for implicit large-eddy simulation of transitional turbulent flows, *J. Comput. Phys.* 336 (2017) 308–329.
- [21] P. Fernandez, N.C. Nguyen, J. Peraire, A physics-based shock capturing method for unsteady laminar and turbulent flows, in: 56th AIAA Aerospace Sciences Meeting, Gaylord Palms, USA, 2018, AIAA–2018–0062.
- [22] B. Fiorina, S.K. Lele, An artificial nonlinear diffusivity method for supersonic reacting flows with shocks, *J. Comput. Phys.* 222 (2007) 246–264.
- [23] S.K. Godunov, The symmetric form of magnetohydrodynamic equations, *Int. J. Numer. Methods Eng.* 1 (1972) 26–34.
- [24] S. Güzey, B. Cockburn, H. Stolarski, The embedded discontinuous Galerkin methods: application to linear shells problems, *Int. J. Numer. Methods Eng.* 70 (2007) 757–790.
- [25] J.S. Hesthaven, T. Warburton, *Nodal Discontinuous Galerkin Methods: Algorithms, Applications and Analysis*, Texts in Applied Mathematics, Springer, 2008.
- [26] G.E. Karniadakis, S. Sherwin, *Spectral/hp Element Methods for Computational Fluid Dynamics*, second edition, Oxford Science Publication, 1999.
- [27] S. Kawai, Divergence-free-preserving high order schemes for magnetohydrodynamics: an artificial magnetic resistivity method, *J. Comput. Phys.* 251 (2013) 292–318.
- [28] S. Kawai, S.K. Lele, Localized artificial diffusivity scheme for discontinuity capturing on curvilinear meshes, *J. Comput. Phys.* 227 (2008) 9498–9526.
- [29] S. Kawai, K.S. Shankar, S.K. Lele, Assessment of localized artificial diffusivity scheme for large-eddy simulation of compressible turbulent flows, *J. Comput. Phys.* 229 (2010) 1739–1762.
- [30] C. Klingenberg, F. Porner, Y. Xia, An efficient implementation of the divergence free constraint in a discontinuous Galerkin method for magnetohydrodynamics on unstructured meshes, *Commun. Comput. Phys.* 21 (2017) 423–442.
- [31] A. Klöckner, T. Warburton, J.S. Hesthaven, Viscous shock capturing in a time-explicit discontinuous Galerkin method, *Math. Model. Nat. Phenom.* 10 (10) (2011) 1–27.
- [32] Alexander Kosovichev, *Lecture Notes in Plasma Physics, Phys.*, vol. 780, February 2015.
- [33] L. Krivodonova, J. Xin, J.F. Remacle, N. Chevaugeon, J.E. Flaherty, Shock detection and limiting with discontinuous Galerkin methods for hyperbolic conservation laws, *Appl. Numer. Math.* 48 (2004) 323–338.
- [34] J.J. Lee, S.J. Shannon, T. Bui-Thanh, J.N. Shadid, Analysis of an HDG method for linearized incompressible resistive MHD equations, *SIAM J. Numer. Anal.* 57 (4) (2019) 1697–1722.
- [35] F. Li, C.-W. Shu, Locally divergence-free discontinuous Galerkin methods for MHD equations, *J. Sci. Comput.* 22 (1) (2005) 413–442.
- [36] F. Li, C.-W. Shu, Locally divergence-free discontinuous Galerkin methods for MHD equations, *J. Sci. Comput.* 22–23 (2005).
- [37] F. Li, L. Xu, S. Yakovlev, Central discontinuous Galerkin methods for ideal MHD equations with the exactly divergence-free magnetic field, *J. Comput. Phys.* 230 (12) (2011) 4828–4847.
- [38] X. Li, M.S. Shephard, M.W. Beall, 3D anisotropic mesh adaptation by mesh modification, *Comput. Methods Appl. Mech. Eng.* 194 (2005) 4915–4950.
- [39] Y. Liu, C.-W. Shu, M. Zhang, Entropy stable high order discontinuous Galerkin methods for ideal compressible MHD on structured meshes, *J. Comput. Phys.* 354 (2018) 163–178.
- [40] P. Londrillo, L. Del Zanna, High-order upwind schemes for multidimensional magnetohydrodynamics, *Astrophys. J.* 530 (2000) 508–524.
- [41] A. Mani, J. Larsson, P. Moin, Suitability of artificial bulk viscosity for large-eddy simulation of turbulent flows with shocks, *J. Comput. Phys.* 228 (2009) 7368–7374.
- [42] A. Mignone, P. Tzeferacos, G. Bodo, High-order conservative finite difference GLM-MHD schemes for cell-centered MHD, *J. Comput. Phys.* 229 (2010) 5896–5920.
- [43] A. Mignone, C. Zanni, P. Tzeferacos, B. van Straalen, P. Colella, G. Bodo, The PLUTO code for adaptive mesh computations in astrophysical fluid dynamics, *Astrophys. J.* 198 (2012).
- [44] D. Moro, N.C. Nguyen, J. Peraire, Dilation-based shock capturing for high-order methods, *Int. J. Numer. Methods Fluids* 82 (7) (2016) 398–416.
- [45] D. Moro-Ludeña, An Adaptive High Order Reynolds-Averaged Navier-Stokes Solver with Transition Prediction, PhD thesis, Massachusetts Institute of Technology, 2015.
- [46] N.C. Nguyen, J. Peraire, B. Cockburn, Hybridizable discontinuous Galerkin methods, in: J.S. Hesthaven, Einar M. Rønquist (Eds.), *Spectral and High Order Methods for Partial Differential Equations*, Springer Berlin Heidelberg, Berlin, Heidelberg, 2011, pp. 63–84.
- [47] N.C. Nguyen, J. Peraire, B. Cockburn, A class of embedded discontinuous Galerkin methods for computational fluid dynamics, *J. Comput. Phys.* 302 (2015) 674–692.
- [48] B.J. Olson, S.K. Lele, Directional artificial fluid properties for compressible large-eddy simulation, *J. Comput. Phys.* 246 (2013) 207–220.
- [49] S.A. Orszag, C.M. Tang, Small-scale structure of two-dimensional magnetohydrodynamic turbulence, *J. Fluid Mech.* 90 (1978) 129–143.
- [50] J. Peraire, N.C. Nguyen, B. Cockburn, An embedded discontinuous Galerkin method for the compressible Euler and Navier-Stokes equations, in: *AIAA Computational Fluid Dynamics Conference*, 2011, AIAA 2011–3228.
- [51] P. Persson, J. Peraire, Sub-cell shock capturing for discontinuous Galerkin methods, in: 44th AIAA Aerospace Sciences Meeting, Reno, Nevada, 2006, AIAA–2006–0112.
- [52] J.M. Picone, R.B. Dahlburg, Evolution of the Orszag–Tang vortex system in a compressible medium. II. Supersonic flow, *Phys. Fluids, B Plasma Phys.* 3 (1) (1991) 29–44.

- [53] K.G. Powell, P.L. Roe, T.J. Linde, T.I. Gombosi, D.L. De Zeeuw, A solution-adaptive upwind scheme for ideal magnetohydrodynamics, *J. Comput. Phys.* 154 (1999) 284–309.
- [54] P.L. Roe, D.S. Balsara, Notes on the eigensystem of magnetohydrodynamics, *J. Appl. Math.* 56 (1996) 57–67.
- [55] K. Schindler, G. Hornig, Magnetic reconnection, in: P. Murdin (Ed.), *Encyclopedia of Astronomy and Astrophysics*, 2001.
- [56] J.M. Stone, T.A. Gardiner, P. Teuben, J.F. Hawley, J.B. Simon Athena, A new code for astrophysical MHD, *Astrophys. J. Suppl. Ser.* 178 (1) (2008) 137–177.
- [57] A. Taube, M. Dumbser, D.S. Balsara, C.D. Munz, Arbitrary high-order discontinuous Galerkin schemes for the magnetohydrodynamic equations, *J. Sci. Comput.* 30 (3) (2007) 441–464.
- [58] G. Tóth, The  $\nabla \cdot \mathbf{B} = 0$  constraint in shock-capturing magnetohydrodynamics codes, *J. Comput. Phys.* 161 (2000) 605–652.
- [59] J. Wurster, M.R. Bate, D.J. Price, T.S. Tricco, Investigating prescriptions for artificial resistivity in smoothed particle magnetohydrodynamics, arXiv: 1706.07721v1, 2017.
- [60] S. Yakovlev, L. Xu, F. Li, Locally divergence-free central discontinuous Galerkin methods for ideal mhd equations, in: *Computational Methods for Hyperbolic Problems*, *J. Comput. Sci.* 4 (1) (2013) 80–91.
- [61] M. Yano, An Optimization Framework for Adaptive Higher-Order Discretizations of Partial Differential Equations on Anisotropic Simplex Meshes, PhD thesis, Department of Aeronautics and Astronautics, Massachusetts Institute of Technology, 2012.